Effect of curing regimes on composition and microstructure of blended pastes: Insight into later-age hydration mechanism

(article starts on next page)

Effect of curing regimes on composition and microstructure of blended pastes: Insight into later-age hydration mechanism

Liming Huang [a,*], Luping Tang [a], Zhijun Dong [b], Birhan Alkadir Abdulahi [a], Zhenghong Yang [c]

[a] *Department of Architecture and Civil Engineering, Chalmers University of Technology, 41296 Gothenburg, Sweden*
[b] *Institute of Technology for Marine Civil Engineering, Shenzhen, Institute of Information Technology, 518172, China*
[c] *School of materials science and engineering, Tongji University, Shanghai 201804, China*

ARTICLE INFO

ABSTRACT

Understanding the hydration of composite binders is essential for decarbonizing the cement industry. This study investigated the microstructure and composition of pastes with either fly ash or slag after different long-term curing. Results show that the elevated temperature slightly reduces the capillary pore volume and internal RH of sealed samples. Water curing largely enhances hydration of fly ash and slag after the first week, forming later-age products in surface zone with stabilized Mc and Hc. This increases both gel and capillary pore volumes. C-A-S-H in water-cured pastes has a longer mean chain length and extremely lower alkali uptake than that in sealed curing. Modelling results indicate that nucleation ceases in sealed pastes once thermodynamic limitations are reached due to self-desiccation. Even with adequate water, late-stage hydration remains kinetically constrained due to the slow nucleation and growth rate near the unhydrated surface, with diffusion likely being one of rate-controlling factors.

1. Introduction

Replacing Portland clinker with supplementary cementitious materials (SCMs) is one of the widely-implementable approach in the cement industry's efforts to reduce CO_2 emissions [1,2]. SCMs and clinker have mutual effects on the hydration reaction of each component to influence the microstructure [3,4], which will finally determine the mechanical performance, moisture and ion transport processes [5–7]. Considerable attention has been devoted to understanding the hydration after the main peak, when the reaction of cementitious materials starts to decrease and then goes to a very slow rate period. This slowing-down occurs despite the fact that belite, slag, and fly ash have a very low hydration degree (often below 10%) [8–10]. As a result, it is rare to achieve complete hydration in both plain Portland cements and SCMs, even after a few years. For instance, Portland cements only reached a maximum hydration degree of approximately 90% after one year [11], while composite cements exhibit even much lower hydration levels [12]. It is still challenging to identify and quantify the rate-limiting factor for the later-age hydration. This limitation hampers the precise assessment and prediction of unreacted portions, which is critical for optimizing the design of concrete.

Since 1948, Powers proposed that the degree of hydration in concrete is determined by the availability of water and pore space [13]. For a complete hydration, concrete must be saturated or nearly so, as hydration products only form in water-filled spaces. Typically, a full hydration of Portland cement requires a minimum water-to-binder ratio (*w/b*) of 0.44, with the additional curing water to reach saturation [14,15]. However, under sealed curing conditions, self-desiccation can occur, reducing the available water in which hydration products can grow. This significantly slows down the hydration rate at later age. Wyrzykowski and Lura [16] observed that reduced humidity due to self-desiccation led to a notable decrease in the hydration rate of sealed samples. Specially, when the *w/b* is <0.3, the internal relative humidity (RH) of cement-based materials can drop below 90% within 3 d [17]. Even with a higher *w/b*, self-desiccation still causes a substantial drop in RH, a phenomenon that becomes more pronounced when the binder is mixed with blast-furnace slag. Briki et al. [18] demonstrated that the internal RH of slag cement with *w/b* of 0.4 droped below 90% after about 7 d. This reduced RH means that liquid water becomes accessible only in nanopores. The refining effect of slag on pore structure increases the volume of gel pores [6,19], leading to more water absorption in these finer pores. In binder systems like limestone calcined clay cement, which features even finer pore sizes than slag binder systems. Although belite in such system remains largely unreacted even after 90 d, the

degree of reaction only showed a slight increases with values below 5% under sealed condition from 90 d to 3 years [20].

The effect of RH on hydration reaction varies depending on the type of minerals. After one-year exposure to water vapor at 20 °C, the estimated minimum RH levels for the hydration of clinker phases are 85% for C_3S, 90% for C_2S, and 60% for C_3A [21]. The hydration process is involved with dissolution of clinker mineral and the subsequent precipitation of hydration products. Flatt et al. [22] found that the negative capillary pressure affected the solubility of alite, so it would cause a stop of hydration when RH was below 80%. At the nanoscale, limited volume of liquid water can alter the crystallization orientation and the critical nucleus size, thereby changing the thermodynamic conditions for crystallization [23]. As the pore sizes decrease to a critical value, this nano-level confinement increases the energy barrier for nucleation [24], which suppresses the rate of nucleation in these small spaces [25]. This constraint has significant influences on hydration in fine pores, particularly in the later stages of the reaction. However, Macie et al. [26] stated that little variation in the supersaturation of pore solution over a period of six months to a year indicated a consistent calcium silicate hydrate (C-S-H) growth mechanism during this time, implying that kinetics of later-age hydration is not constrained by pore-space effects. Although confinement within large gel pores may not drastically affect the size of primary nuclei, it notably impacts the activity of water, influencing the nucleation process [27,28]. Despite its importance, the influence of water activity and confinement at the nanoscale on nucleation has not been fully explored in previous investigations.

Even when adequate moisture is offered by the water curing, the hydration of belite in a binary system could only approach full hydration after 1 year at elevated temperatures (30–60 °C) [29]. Snellings et al. [30] demonstrated that the bound water content in samples cured at various temperatures converged to the same value after 180 d of the seal curing. Interestingly, while elevated temperature curing had negligible affect the hydration degree of slag at later stages, it did reduce the formation of portlandite and ettringite, largely due to accelerated reactions during the early stages. Binders cured under low temperatures (<25 °C) exhibited higher bound water content and compressive strength at later ages compared to those cured at relatively high temperatures (>30 °C) [31,32]. This intriguing phenomenon suggests that low-temperature curing may foster more favorable conditions for long-term hydration, challenging the conventional understanding that elevated temperatures accelerate hydration and improve long-term performance.

Despite of relevant research efforts mentioned above, the mechanisms governing the later stage hydration remain poorly understood. Berodier and Scrivener [33] proposed that "lack of space" became limiting factor for the hydration kinetics after the initial few days. The space limiting effect is more pronounced in binders with higher SCMs content, such as calcined clay limestone system with 50% cement replacement [34]. Some studies, however, have shown that denser inner hydration products may hinder later-age hydration by impeding the diffusion of ions from the surface to reaction site. The formation of a dense C-S-H around unhydrated clinker particles, known as inner hydration products [35,36], limits the space available for the hydration near the surface of particles. This zone is highly impermeable, making it difficult for ions and water to diffuse through. In slag-blended systems, the phase distribution within the inner part indicates that both the diffusion of dissolved ions from the slag surface and the availability of pore space are critical factors for the later-age reaction of slag [37,38]. At this point, diffusion may become the limiting factor in later-stage hydration. Bullard et al. [39] suggested that the rate of product growth controls the reaction rate until congestion occurs in the capillary pore space. Scrivener et al. [40] argued that diffusion is not the controlling mechanism; instead, they emphasized the absence of water-filled pores larger than approximately 10 nm, and the depletion of anhydrous material as key factors contributing to the decline in reaction rate.

Building upon the current ambiguous understanding of hydration

mechanism at later age, we conducted an in-depth investigation into the microstructure of blended pastes containing either fly ash or slag. In this study, pastes were subjected to three different curing regimes to assess effects of water availability and temperature on hydration at later age (after one week and about one year). The microstructure and phase composition of hardened pastes were thoroughly characterized using advanced measurement techniques. In the final discussion section, we will elucidate the mechanisms responsible for the slowdown and cessation of hydration at the later ages with respect to different curing conditions, by modelling of the thermodynamics and kinetics of precipitation in nanopores.

2. Experimental information

2.1. Materials and procedures

The cementitious materials include Portland cement (CEM I 52.5R), fly ash sourced from Cementa and slag obtained from Thomas Cement. Table 1 presents the chemical compositions of these binders, which were measured by X-ray Fluorescence and particle size distributions are provided in [41]. Portland cement was substituted with either 35% fly ash (P145) or 35% slag (P245) by mass to form the blended binder systems. Pastes were prepared with a *w/b* of 0.45. The details of mixing procedure were described in the previous publication [41].

Pastes were subjected to three different curing regimes (see Fig. 1). Some paste was cast in polypropylene tubes and sealed with lids. One batch of the tubes was cured under a constant temperature with 20 ± 1 °C for 600 d. The other batch of tubes were put at 20 °C until 390 d, then wrapped with three layers of water-proof films and sealed with tape, moved into an oven with 50 °C until 600 d, which is noted as HT. Other pastes were cast into zip bags and rolled to a uniform thickness of approximately 1 mm. After the first week of sealed curing, these samples were crushed and then sieved through 1 mm meshes, and cured in water with liquid to solid (L/S) mass ratio of 1 up to 600 d.

For microstructural analysis, the sealed samples were crushed into fragments and then were immersed into the isopropanol for 3 d. Following the recommendation in [42], samples were rinsed with diethyl ether before subjected to the vacuum drying at 30 °C for 24 h. The dried samples were stored in sealed plastic tubes for the further test.

2.2. Methods

2.2.1. XRD

X-ray diffraction (XRD) of powder samples was tested by the D/max 2550 VB3+/PC diffractometer (Rigaku International Corporation) with a monochromatic Cu Kα radiation (λ = 1.5408 Å). Measurements were conducted in the range of 5–45° (2θ) with a step of 0.1°, a counting time of 1 s/step, a tube voltage of 40 kV and a current of 100 mA.

2.2.2. TGA

The weight loss during heating was measured by a

Table 1
Chemical compositions of binders by weight percentage (with uncertainty of ~4%).

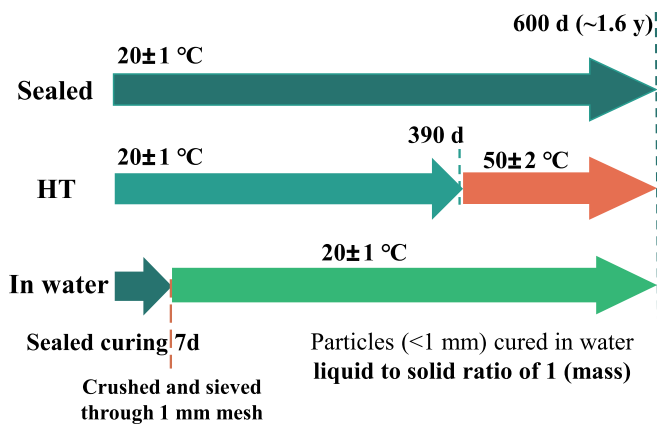| Chemical composition	CEM I 52.5 R	Slag	Fly ash
CaO	62.2	39.11	5.1
SiO_2	19.6	36.63	54.6
Al_2O_3	4.5	13.56	22.4
Fe_2O_3	3	0.49	8.7
SO_3	3.5	0.27	0.8
MgO	3.5	8.52	1.8
K_2O	1.01	0.57	2.1
Na_2O	0.27	0.42	1
Cl	0.07	0.009	–
LOI	2.5	0.421	3.5

Fig. 1. Curing regimes of the blended pastes.

thermogravimetric and differential thermal analysis instrument (SDT Q600, TA Instruments) with a Stanton Redcroft STA 780 simultaneous thermal analyzer. Two parallel tests of each sample were operated with an initial mass of about 20 mg, heating at a rate of 10 °C/min under a continuous nitrogen flow (50 cm^3/min) from 20 °C to 1000 °C. The amount of bound water and portlandite is calculated by "Tangential methods" [43] with respect to the initial sample mass.

2.2.3. NMR

Solid state ^{29}Si magic-angle-spinning (MAS) NMR measurements were conducted using a JEOL ECZ600MHz (14.1 T) spectrometer, For the assessment of silicate polymerization in hydration products. The samples were enclosed inside 8 mm ZrO$_2$ rotors, spinning at a rate of 5 kHz and $\Upsilon B/2\pi = 40$ kHz. Parameters for relaxation delay and scanning numbers were set at 60 s and 1024 times, respectively. Chemical shifts were referenced to trimethylsilyl (TSPA). The deconvolution has been done within Origin software.

2.2.4. MIP

The pore size distribution in fragment particles was measured by mercury intrusion porosimetry (MIP), using a MicroActive AutoPore V 9600 Version 2.03 machine. The pressure was initiated at 0.003 Pa and then increased up to 250 MPa, which allows intrusion of pore entries from initially 373 µm down to about 6 nm (contact angle 138°). It should be noted that MIP measurements are only useful to provide threshold diameters and intrudable pore space measurements [44], so this study used it as comparative indices for the pore connectivity and porosity in hydrated cements.

2.2.5. N$_2$ sorption

A gas adsorption analyzer (TriStar3000, Micromeritics) was used to measure the nitrogen sorption isotherm of samples. Before the sorption measurement, samples were outgassed for 4 h with a continuous N$_2$ gas flow at 60 °C for a fast water removal. Adsorption isotherms were measured over the pressure range of 0.01–0.982 P/P_0 with an equilibrium interval of 10 s for each step at 77 K. Each sample has been repeated at least once, and the final value is an average of parallel tests. It should be noted that the drying treatment will cause dynamical structural change of C-A-S-H and N$_2$ gas is hardly to penetrate into small gel pores [19], so we used water vapor desorption below 35% RH as a supplementary test for analyzing specific surface aera and gel pores.

2.2.6. Water vapor desorption

The sealed curing pastes were crushed into particles (<2 mm) and then conditioned in the box with different RHs (33%, 23%, 11% and ~3%) at 20 ± 1 °C, controlled by the saturated salt solution of MgCl$_2$, CH$_3$COOK, LiCl and silica gel respectively [45]. Calcium hydroxide was put in the climate box as a sacrifice to absorb CO$_2$. The RH in the

conditioning box was monitored by the RH sensors (testo 174H). The mass change of each sample was measured at about each week, and it is assumed to reach equilibrium state when the weight loss rate is lower than 0.0001%/day.

2.2.7. BSEM

The fragments were vacuum impregnated with low viscosity epoxy resin. Specimens were then polished with a decrease grade of SiC papers from 600 to 1200 mesh, followed with polishing with diamond crystallites from 3 to 0.25 µm. The polished surface plated with Au were examined by Quanta 200 ESEM FEG from FEI under backscatter scanning electron microscopy (BSEM), with an accelerating voltage of 15–20 kV, coupled with an energy dispersive X-ray spectrometer (EDS) to collect local composition information.

2.2.8. Internal RH

After 600 days of curing, the samples sealed in tube were quickly crushed into fragments and then sealed in a triple layer zip bag with a humidity meter inside (Testo 174H). The zip bags were put in a sealed bucket (500 mL) to ensure a fast equilibrium between sample and stagnant air. The meter continuously records the temperature and the RH inside the bags every hour. The equilibrium time of each measurement is about 5 d. The RH of each sample was the average value of three parallel tests.

2.2.9. Thermodynamic modelling

Thermodynamic modelling was carried out using GEM-Selektor v3.7, a freely available software for Gibbs energy minimization. The simulation was based on the cement database Cemdata18 [46] and the PSI-GEMS thermodynamic database [47]. The activity coefficients of aqueous species were calculated using the built-in extended Debye-Hückel equation, as fully referenced in [48]. It was applied to simulate the influence of temperature and hydration degree on the phases of calcium silicate hydrate.

3. Analysis of results

3.1. Phase composition

3.1.1. XRD and TGA

Fig. 2 shows the composition of hydration products measured by XRD and TGA. The weight loss at specific temperature ranges was attributed to the decomposition of hydration phases based on a microstructural analysis book [43]. In particular, the weight loss between 300 and 400 °C corresponds to the dehydration of jennite and calcium aluminosilicate hydrate (C-A-S-H) [49,50]. XRD analysis identified portlandite, calcium monocarboaluminate (Mc), quartz and calcite in fly ash blended paste under sealed curing (Fig. 2a). The inert quartz phase is originally from the fly ash as confirmed by XRD of raw materials (see supplementary information). A weak diffraction peak from belite was also detected. Alite and calcium aluminate phase were mostly depleted, with no evident peak observed for these phases after 600 d of curing. The crystalline phases in slag-blended paste are very similar to those in fly ash paste except for the absence of quartz (Fig. 2b). The change in peak intensity suggests that elevated temperature curing after 390 days causes a reduction in the amounts of both Mc and portlandite in the fly ash paste. A minor reduction in portlandite content shown by peak intensity is also supported by the TGA data (Fig. 2c).

Previous studies have demonstrated that Mc forms at the expense of ettringite. When pastes are initially cured at 50 °C, the amount of Mc is lower compared to that in samples cured at 20 °C [31]. Higher curing temperatures increase the solubility of ettringite and calcium monosulfoaluminate (AFm), while promoting the incorporation of sulfate into C-A-S-H [51,52]. Consequently, the curing after one year at 50 °C likely reduces Mc content while increasing the mass of C-A-S-H. A similar reduction in Mc content due to elevated curing temperature is observed
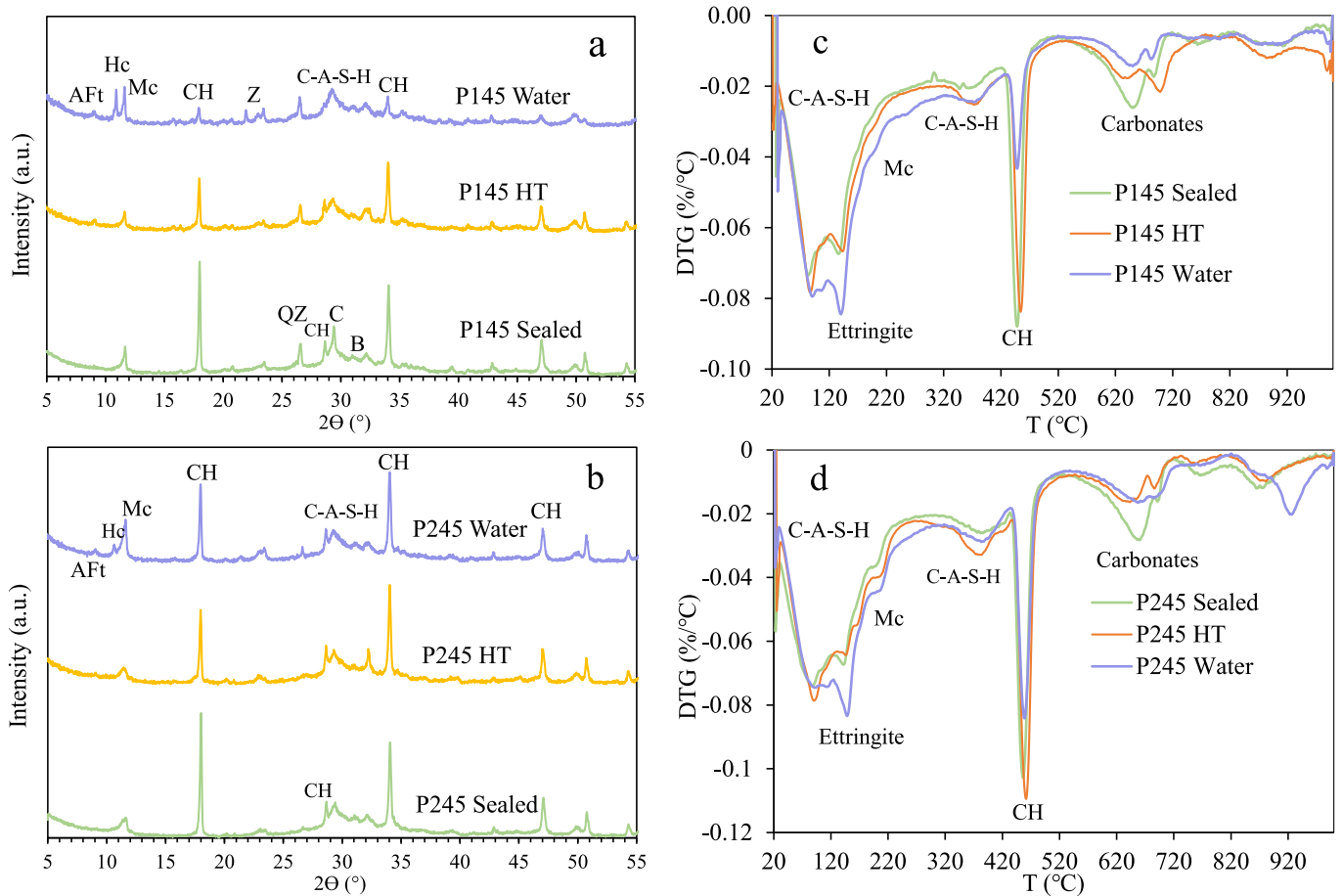
Fig. 2. The composition of pastes measured by XRD and TGA: AFt-Ettringite, Hc- Calcium hemicarboaluminate, Mc- Calcium monocarboaluminate, CH-Portlandite, Z-Zeolite, B-Belite, C-Calcite, QZ-Quartz.

in slag-blended paste. However, in contrast to the fly ash system, the amount of portlandite in the slag-blended paste seems to show a little increase after high-temperature curing (Fig. 2d and Table 2). The difference between fly ash and slag paste can be attributed to the activated latent-hydraulic reaction of slag by elevated temperature. A similar trend was noted in slag-blended pastes when curing ages was prolonged after 28 d [53].

When blended pastes were cured in water after 7 d, the hydration degree of fly ash is much higher than those cured under sealed condition. This is evidenced by the large increase in chemically bound water and the notable reduction in portlandite content detected by both XRD and TGA analyses. As shown in Table 2, in the fly ash paste subjected to water curing, the portlandite content was reduced to 4.7(±0.2) %, approximately half of that observed in the sealed curing paste. With sufficient water, fly ash undergoes further dissolution and reaction with calcium source, leading to a reduction in portlandite and increase in C-A-S-H content. This results in a bound water of 15.49%, which is higher than that of pastes cured under sealed conditions. In the slag blended paste, the enhanced later-age hydration by water curing reduces the portlandite content to 9.6(±0.5) %. The chemically bound water in the water-cured slag pastes is also significantly higher than those under

sealed conditions. Notably, slag pastes exhibit higher amounts of bound water and portlandite compared to fly ash pastes across all curing conditions. This difference can be attributed to variations in phases assemblage, with the slag-blended pastes containing higher bound water content than fly ash blends at the same age [54,55]. Moreover, a higher fly ash use tends to decrease the chemically bound water [56].

In the water-cured samples, zeolite was detected in the fly ash paste. Peaks corresponding to calcium hemicarboaluminate (Hc) were observed in both fly ash and slag blended pastes, with significantly higher intensity in the fly ash paste. The presence of small amounts of calcite in CEM I can change the mineralogy of AFm phases, leading to the formation of Mc and Hc [57,58]. The stability of those phases depends on several factors, including ion types in solution, temperature, and water activity. Hc can be stabilized by the sulfates and chlorides in the pore solution [59]. According to the chemical composition of raw materials, fly ash contains a higher content of sulfate compared to slag. Previous studies have shown that as the replacement (hydration) level of fly ash increases, the formation of Hc becomes more favorable than Mc [60,61]. Thermodynamically, Hc forms at room temperature (around 20 °C) when the fly ash hydration degree reaches between 30% and 40%, and it remains stable when the hydration degree of slag exceeds

Table 2
Chemical bound water and portlandite content with respect to the initial mass of dry paste.

Samples	P145			P245		
	Sealed	HT	In water	Sealed	HT	In water
Bound water	11.0(±0.9)%	12.0(±0.5)%	14.5(±1)%	12.8(±0.7)%	13.1(±0.8)%	15.2(±1)%
Portlandite	8.9(±0.4)%	8.6(±0.5)%	4.7(±0.2)%	10.9(±0.6)%	11.8(±0.6)%	9.6(±0.5)%

60% [19]. It is evident that the water curing at later ages can stabilize both Mc and Hc phases. The effect of temperature and water activity (relative humidity) on the stability of AFm-carbonates, however, remains an intriguing and unresolved issue, which is beyond the scope of this paper but warrants further investigations.

3.1.2. NMR

Solid-state magic-angle-spinning (MAS) NMR spectroscopy is widely used to evaluate the hydration degree of minerals in Portland cement and SCMs [4]. Additionally, it provides valuable information for the structural characteristics of C-A-S-H [62]. Fig. 3 shows the results of ^{29}Si MAS NMR analysis of blended pastes cured under three regimes. Peak deconvolution was performed using peak positions identified in previous studies [63,64]. Specifically, monomeric Q0 (-70.5 to -75 ppm) signals correspond to silicates in cement and SCMs, and Q4(Al) (-107 to -108.5 ppm) is associated with unhydrated fly ash. Other peaks are attributed to silicate chains in C-A-S-H, including dimers Q1(-78.3 to -78.5 ppm), bridging Q2b(Al) (-80.3 to -82.0 ppm) and non-bridging Q2 (Q2pa, -84.1 to -84.6 ppm; Q2pb, -86.5 to -87 ppm). To assess the connectivity of silicate chains, the mean chain length (MCL) was calculated following Richardson's methodology [64,65]. Typically, MCL increases as the Ca/Si ratio decreases in the C-A-S-H structure [66,67].

The Q0 signal (at -71.33 ppm [68]) associated with belite in the fly ash blended paste, is noticeably weaker in water-cured samples compared to those cured under sealed conditions. The Q4 peak, representing cross-linked aluminosilicates in fly ash, also shows a reduction when the paste was cured at elevated temperatures and in water. These findings suggest that the later-age hydration of both belite and fly ash has been enhanced by the increased temperature, but the enhancement is limited by water availability. Notably, water curing has a stronger effect on later-age hydration than temperatures. For slag blended pastes, the belite peak overlaps monomer signal from slag; however, the overall Q0 peak area was significantly lower in water-cured than that in sealed curing samples.

Blending of fly ash and slag typically results in the formation of C-S-H with a lower Ca/Si ratio compared to pure Portland cement. Aluminum (Al) can be incorporated into the C-S-H structure, primarily at the bridging sites in the silicate chains to form a C-A-S-H structure [69,70]. A reduction in Ca/Si ratio creates more vacancies in the structure, allowing for an increased Al uptake in the C-A-S-H. This is particularly evident in samples with enhanced later-age hydration, where the percentage of Q2b(Al) increases, after curing at elevated temperatures or in water. As the reaction degree of fly ash increases, dimers within the C-A-S-H structure are connected by bridging Al or Si, leading to a reduction in Q1 and the formation of more polymerized silicate chains with higher MCL. Consequently, the MCL values for fly ash pastes are observed as 2.67 for sealed curing, 3.06 for HT, and 4.05 for water curing. Due to the higher calcium content in slag that reduces the connection of silicate, C-A-S-H in slag pastes contains more Q1 than fly ash pastes under the same curing regime. In general, C-A-S-H formed in fly ash pastes tends to have a lower Ca/Si ratio and higher Al content than that found in slag blends [71,72]. High-temperature curing appears to slightly enhance the
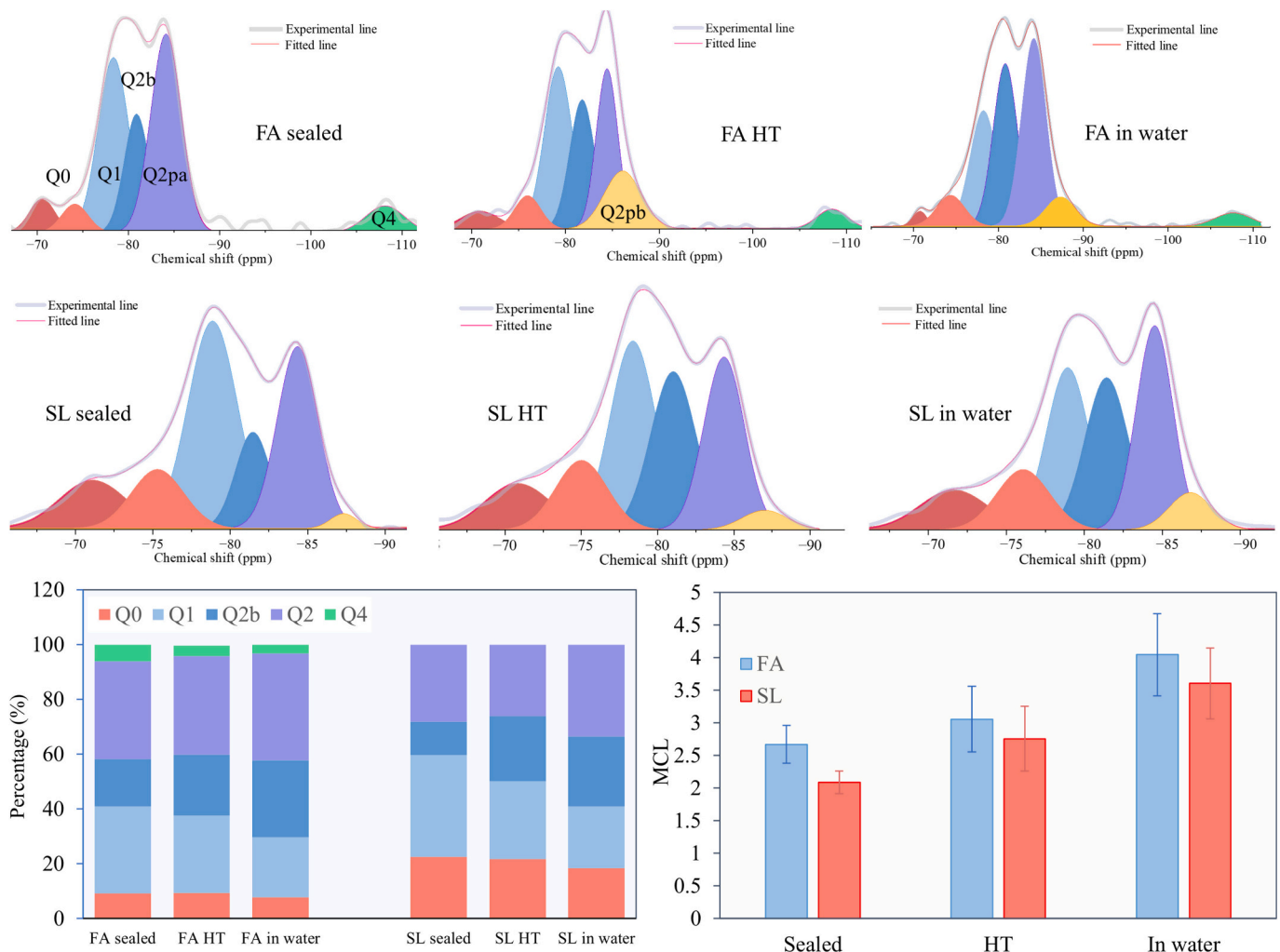

Fig. 3. Solid NMR data of fly ash (FA) and slag (SL) blended pastes cured under different regimes and the analysis of silicate polymerization state.

hydration degree of sealed pastes, but it still alters the polymerization of silicate chain. Water curing has a more pronounced effect on later-age hydration reactions. However, a significant portion of both fly ash and slag still remains unreacted. It has been noted that slag does not achieve the complete hydration even after 20 years, as evidenced by residual slag grains in long-term studies [73]. Thus, we conclude that even with sufficient water availability, hydration eventually halts at a certain level. This will be discussed in detail in the last section.

3.2. Microstructure

3.2.1. MIP

Fig. 4 shows the pore size distribution of hardened pastes measured by MIP. This section provides a comparative analysis of pores with diameter larger than 6 nm. As observed from the compositional changes, elevated temperature slightly enhances the hydration of blended pastes under sealed curing condition. In the case of fly ash pastes, the increased hydration due to higher temperature results in a reduction in the volume of pores with critical entry diameter between 20 and 50 nm. This suggests that enhanced hydration after 390 d has partially filled these pores to form pores with smaller entry diameters in the range of 6–20 nm. However, despite this shift in pore sizes, the total volume of pores larger than 6 nm remains almost unchanged at elevated temperature. Slag-blended pastes show a similar reduction in the volume of large capillary pores (20–100 nm) after curing at 50 °C. However, the increase in smaller pore volumes (6–20 nm) is negligible, leading to a lower overall pore volume compared to samples cured at room temperature. Fly ash pastes generally show higher intrudable pore volumes than slag pastes with the same *w/b*, which is consistent with observations from previous studies on samples cured for one year [6].

Water curing after 7 d significantly affects the microstructure of pastes, resulting in a substantially higher pore volume compared to samples cured under sealed conditions, across a wide pore size range from 6 to 100 nm. A long-term immersion in water or solution can lead to calcium leaching from pastes, which may coarsen the pore structure [74,75]. However, as illustrated in the experimental section, the water to paste mass ratio was carefully controlled at 1, which reduces the extent of leaching compared to the referred studies. More importantly, a notable increase in hydration degree was detected through composition tests (Figs. 2 and 3), contributing to the formation of additional C-A-S-H with gel pores. Further insights into how leaching and transport processes influence the microstructure of the hardened pastes will be discussed in section 3.2.4, based on BSEM analysis. It is important to note that the total intrudable pore volume measured by MIP excludes pores smaller than 6 nm. To further examine these smaller pores, N_2 sorption data will be discussed in the next section.

3.2.2. Pore structure by N_2 sorption

Fig. 5 illustrates the nanopore structure of dried pastes measured by N_2 sorption, a method widely used to characterize the pore size distribution of hardened cement pastes [76,77]. The sudden drop in desorption curves is primarily due to the cavitation, which only occurs during the desorption process [78]. Two distinct cavitation processes were detected at relative pressures (P/P0) of 90%–95% and 45%–50%, respectively. The stronger hysteresis observed at P/P0 around 45% in water-cured samples indicates a higher volume of complex gel pores. This results from a higher hydration degree, as indicated from Fig. 2 and Fig. 3, to form more C-A-S-H with small gel pores [19,79].

The pore size distribution calculated using the BJH model is able to check the change of gel pore smaller than 6 nm, which were not captured by the MIP analysis discussed in the previous section. Both adsorption and desorption data show that the elevated temperature
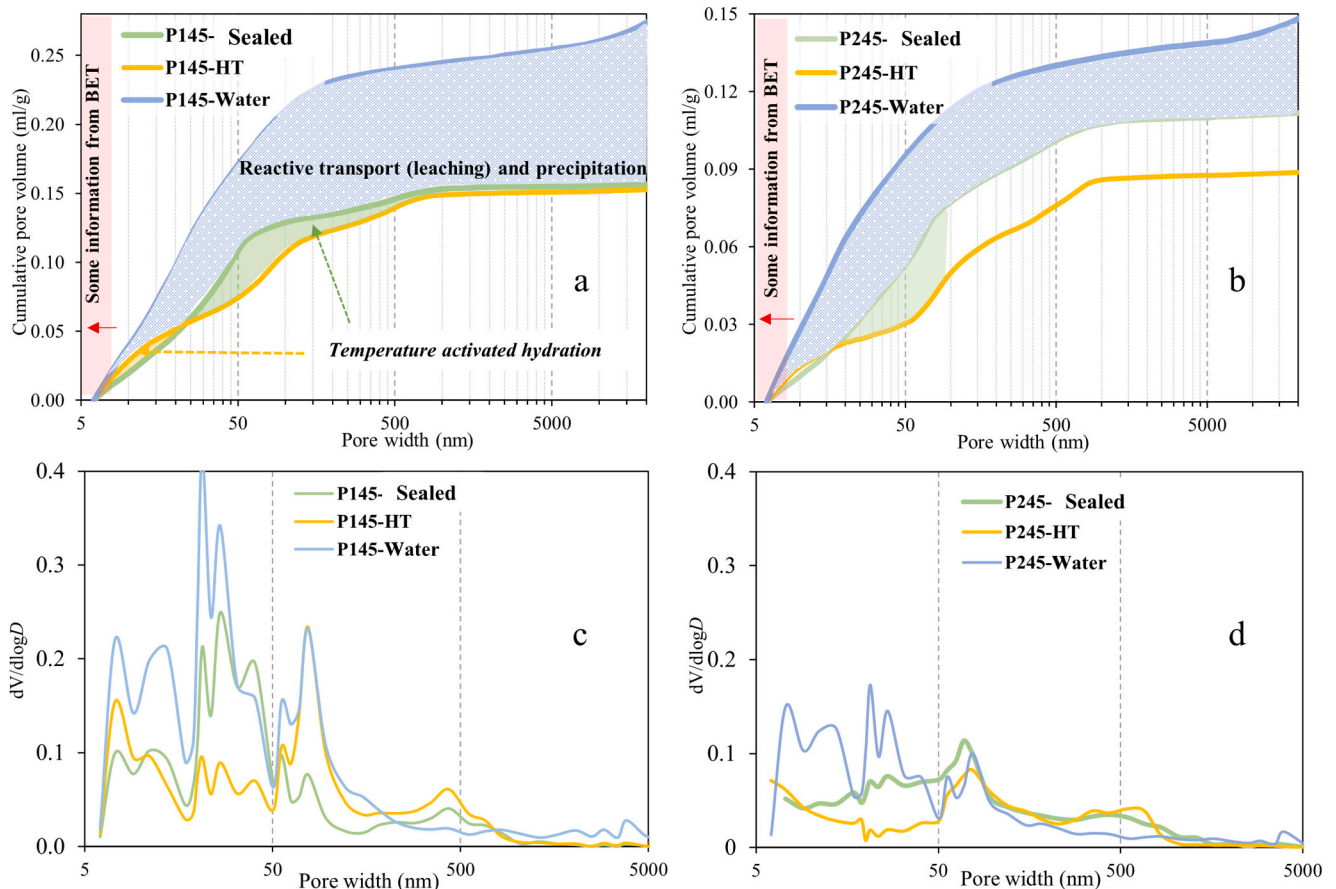

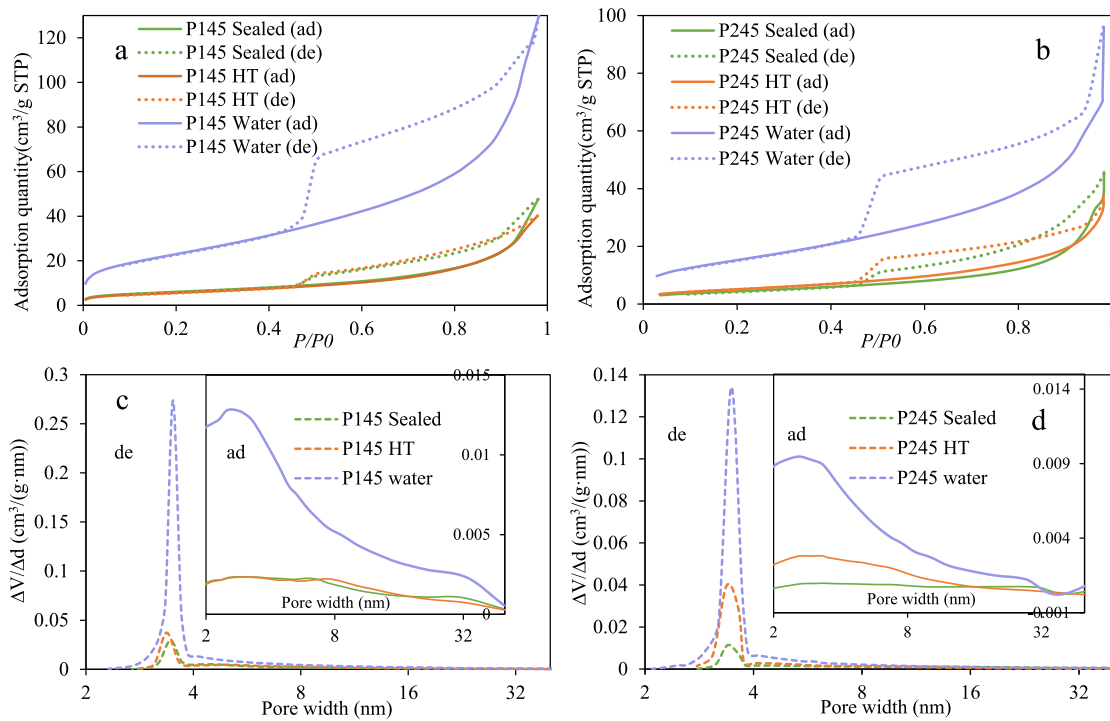**Fig. 4.** Pore size distribution of blended pastes tested by MIP.

Fig. 5. N₂ adsorption (ad) and desorption (de) data, and pore size distribution calculated by sorption data. The deviation of two parallel tests is about 8%.

curing of fly ash paste has very limited effect on the volume of these gel pores. However, for the slag blended pastes, the MIP results showed a reduction in the total volume of pores larger than 6 nm, whereas N₂ sorption reveals a noticeable increase in the volume of gel pores smaller than 8 nm after elevated temperature curing. This means that the decreased capillary pores were filled with later-age hydration products, forming some finer gel pores. The discrepancies of gel pore change in fly ash paste and slag paste are related to differences in internal RH and calcium content, which influence the nucleation of hydration products at later-age.

3.2.3. Water vapor desorption

The microstructure of C-A-S-H is highly sensitive to the moisture content, with drying treatments inducing dynamic changes in gel pore structure [80,81]. Water vapor sorption data is therefore crucial for complementing the information of gel pore structure at moist state. As molecular dynamics modelling has shown [82], the moisture in cement-based materials equilibrated at 20–25 % RH primarily corresponds to water confined within interlayers of C-A-S-H. Fig. 6 illustrates the moisture desorption in samples equilibrated below 35 % RH levels. Due to the mesoporous structure of C-A-S-H, the moisture in this RH range can be used as an indicator of C-A-S-H content, assuming a similar layer structure [19].

For samples cured at 20 °C, sufficient water curing at later age results in a higher amount of C-A-S-H compared to the sealed curing. Water

curing seems to have a more pronounced effect on the content of C-A-S-H gel products in slag blended paste than that in fly ash blended paste. For samples cured at 50 °C after 390 d, the moisture content at RH below 35% is lower compared to that of room-temperature samples, so it appears to indicate a lower content of gel products. However, elevated temperatures cause water migration from interlayers into gel pores, leading to structural changes [83]. Long-term exposure to high temperature reduces structural water within C-A-S-H [84]. Therefore, evaluating C-A-S-H content for samples cured at different temperatures requires additional consideration of these structural changes. As indicated by bound water results in Fig. 2 and Table 3, samples cured at 50 °C showed a slight increase in hydration products compared to room-temperature-cured samples, Apparently, the structural water content of C-A-S-H in blended pastes decreases at elevated temperatures.

The specific surface area (SSA) of the moist pastes was determined using water vapor desorption data within the BET theory [85]. The method for calculating SSA from water vapor desorption data is detailed in a publication by Belie et al. [86]. Generally, the SSA of sealed fly ash samples shows a small variation between room and elevated temperatures, indicating that the limited increase in hydration under elevated temperature conditions with a marginal change in the formation of high SSA phases like C-A-S-H. The fly ash-blended samples cured in water, however, exhibit a significantly higher SSA (251.39 m²/g) compared to sealed samples. For slag-blended pastes, there are notable differences in SSA of samples under various curing regimes. Sealed slag sample has an SSA of 210.84 m²/g, which increases to 220.77 m²/g under elevated
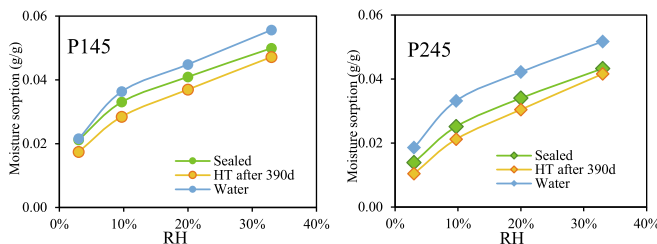

Fig. 6. Water vapor desorption isotherm below 35% RH.

Table 3
Specific surface area (SSA) of pastes calculated from water vapor sorption data.

Samples	SSA by H₂O (m²/g)
P145 Sealed	220.95
P145 HT	218.50
P145 Water	251.39
P245 Sealed	210.84
P245 HT	220.77
P245 Water	239.82

temperature conditions (HT) and 239.82 m²/g in water curing. These results confirm the influence of different curing regimes on the hydration degree of binders, as discussed in previous sections, highlighting the greater enhancement of hydration in water-cured samples.

3.2.4. BSEM

BSEM coupled with EDS element mapping is a powerful tool for analyzing the microstructure and hydration phases in blended binders [4]. Fig. 7 and Fig. 8 provide BSEM images of pastes containing fly ash and slag, respectively, after different long-term curing regimes. The hydration degree of fly ash, particularly for large particles (> 50 um), is noticeably limited under sealed curing conditions (Fig. 7a and b). In contrast, the paste subjected to elevated temperature has a denser structure than that cured at room temperature. This aligns with the MIP results, which show a reduction in the volume of large capillary pores after elevated temperatures. This observation is also consistent with previous studies, which demonstrated that increasing the curing temperature up to 90 d enhances the density of fly ash mortars and improves their compressive strength [32]. In slag-blended pastes (Fig. 8a and b), characteristic hydration rims are identified, which correspond to the formation of hydrotalcite-like phases resulting from localized precipitation. The microstructure features of slag pastes under sealed conditions are relatively similar under BSEM, regardless of whether the curing occurred at room temperature or elevated temperatures.

While curing in water, both fly ash and slag particles show a higher reaction degree, as evidenced by a greater dissolution of particles compared to the sealed curing samples. A loose surface layer, noted as later-age zone, can be observed in water-cured samples, characterized by the presence of ettringite (AFt) with long needle-like structures (Fig. 7c and d). These zones contain not only calcium silicate hydrates but also a substantial amount of AFm (carbonate) phases, explaining the strong XRD diffraction peaks of Mc and Hc in water-cured samples (Fig. 2). Interestingly, the loose layer is not uniformly distributed across all particles but appears in localized regions on particle surfaces. In slag blends cured in water, numerous small particles are interconnected by hydration products formed at later ages (Fig. 8c). This suggests that these loose surface zones are mainly a result of enhanced later-age hydration rather than a leaching effect alone. The sufficient water provided by moist curing facilitates the dissolution of unhydrated fly ash, slag, and clinker, promoting diffusion of ions from the inner pore solution to the surface, where supersaturation leads to nucleation and growth of later-stage hydration products. The formation of these later-age zones causes a much higher intrudable pore volume in MIP test and a stronger cavitation in the N₂ sorption test shown in previous sections.

To further investigate the composition of hydration products near fly ash and slag particles, three zones (Z1–Z3, Fig. 7) were randomly
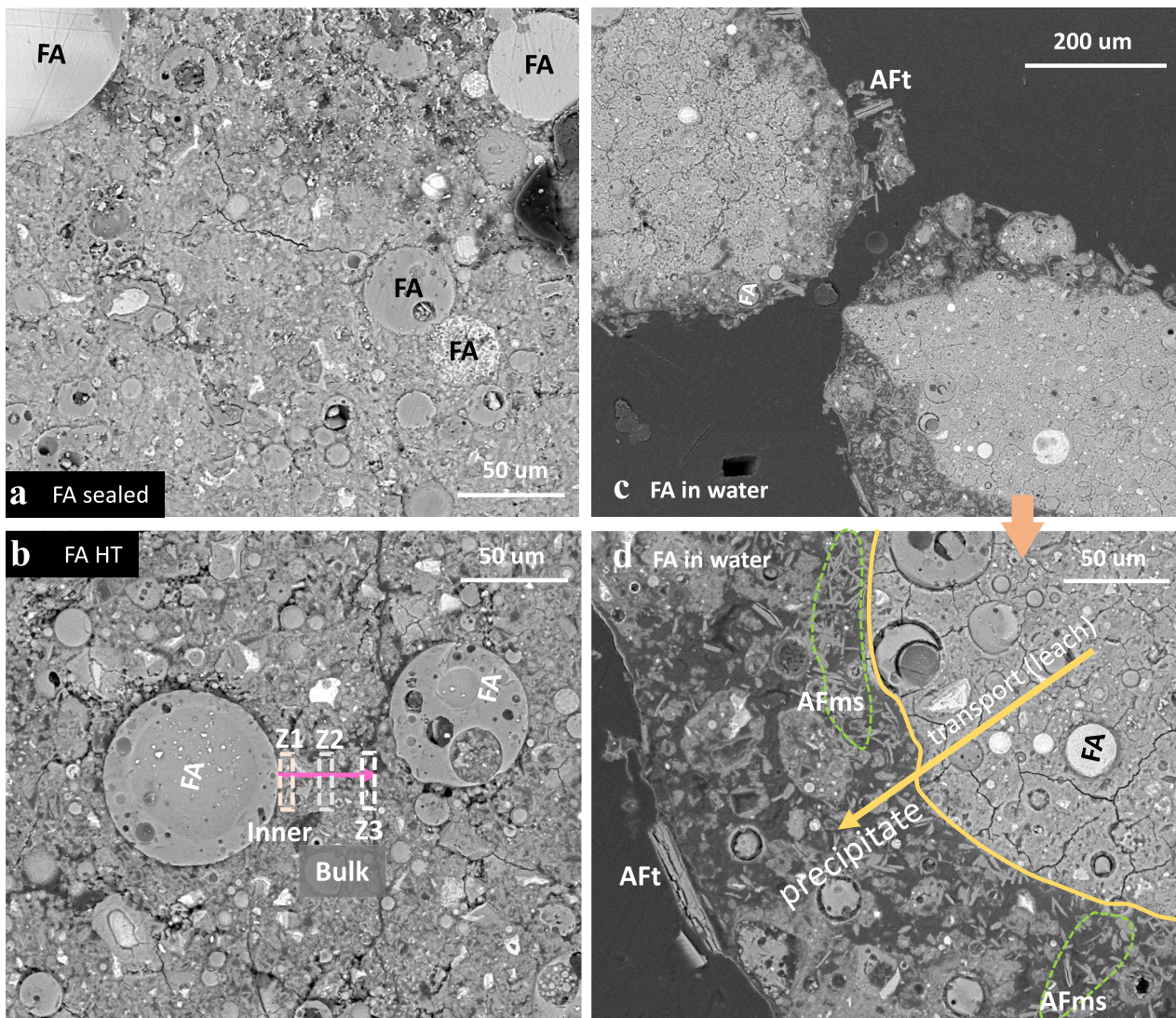

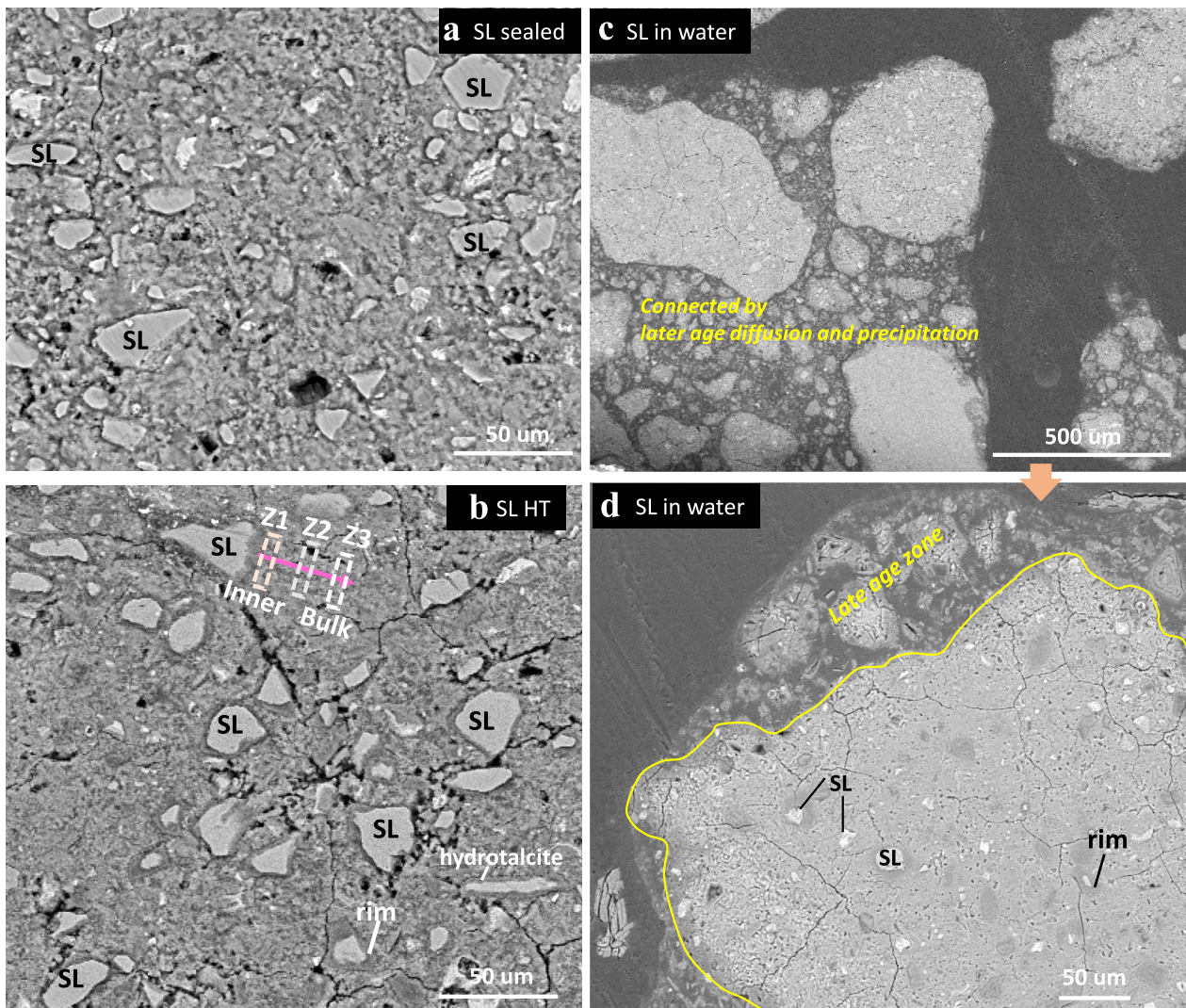**Fig. 7.** BSEM images of pastes containing fly ash subjected to different curing regimes.

Fig. 8. BSEM images of pastes containing slag subjected to different curing regimes.

selected at different distances from the unhydrated surface (~5 μm, 25 μm, and 50 μm) for EDS point analysis. It should be noted that the grains in the early-age zone were chosen for the analysis of water-cured samples. The statistical data in Fig. 9 is based on the analysis of a minimum of two unhydrated grains per sample, with four points assessed in each zone. Using Richardson's C-S-H structural model [87], the structural characteristics of C-A-S-H in hydration products were interpreted referring to two representative tobermorite (T) units: one with 11 tetrahedra (T11), where aluminum occupies one of the three bridging sites, and the other with infinite chain lengths (T∞).

For the sealed samples, hydration products in Z3 of fly ash blends have a wide Ca/Si ratio (1.33 to 5, Fig. 9a), and points with the high Ca/Si (> 2) ratio likely imply a mix of portlandite and C-A-S-H. The Ca/Si ratios of Z1-Z2 in sealed samples stays in 1.33–0.83, aligning with compositions of jennite and T11 (Al). After curing at 50 °C (HT), hydration products in Z1 of fly ash particle has a Ca/Si < 0.67, along with Al/Ca > 0.4 and Al/Si about 0.25. On average, C-A-S-H in these blended pastes shows Ca/(Si + Al) ratios of 1.5–1.9 [88], occasionally decreasing to 1.33 in blends with silica fume [89]. Even with increasing silica fume content, the Ca/Si ratio of the inner C-S-H rim rarely drops below ~1.0, which was only formed in the absence of portlandite at later ages [90]. Therefore, the products in Z1 with such a low Ca/Si have a very different structure than C-A-S-H. The characteristic composition (Fig. 9b) is very similar to alkali-silica reaction (ASR) gel, which has a (Na + K)/Ca > 0.2

and Si/Ca > 2 [91], However, further research is necessary to fully identify the structure of these products.

For water-cured fly ash samples, the hydration products show a lower Ca/Si ratio, in the range of 1.0 to 1.33, compared to sealed curing samples. Interestingly, the (Na + K)/Ca ratio in sealed samples from both curing temperatures follows a linear correlation with Si/Ca, which can be described by the equation $y = 0.42x–0.095$. In contrast, the alkali content in the C-A-S-H structure of water-cured fly ash blends is significantly lower, with a (Na + K)/Ca ratio below 0.03. This suggests a diffusion or leaching of alkalis from the inner pore solution to the surface zone.

Fig. 9c shows that hydration products around slag particles have a Ca/Si ratio ranging between 1.0 and 1.3, and an Al/Ca ratio between 0.1 and 0.4, under sealed conditions at room temperature. The alkali content in these hydration products is highest (Fig. 9d) compared to other two curing regimes, with (Na + K)/Ca value between 0.1 and 0.35. After elevated temperature curing, some points show very low Si/Ca ratios (< 0.5) but high (Mg + Fe)/Ca ratio. A large portion of inner products has a Si/Ca ratio of 1.1–1.4, with (Na + K)/Ca of 0.1–0.2. This suggests the coexistence of C-A-S-H with sodium- and aluminum-substituted calcium silicate hydrates (C-(N)-A-S-H) and sodium aluminosilicate hydrate (N-A-S-H) gels [92]. In the water-cured samples, the Si/Ca ratio of hydration products near slag particles ranges from 0.4 to 1.15. Several points exhibit Al/Si ratio close to 0.5 and (Mg + Fe)/Ca ratio > 0.4, reflecting
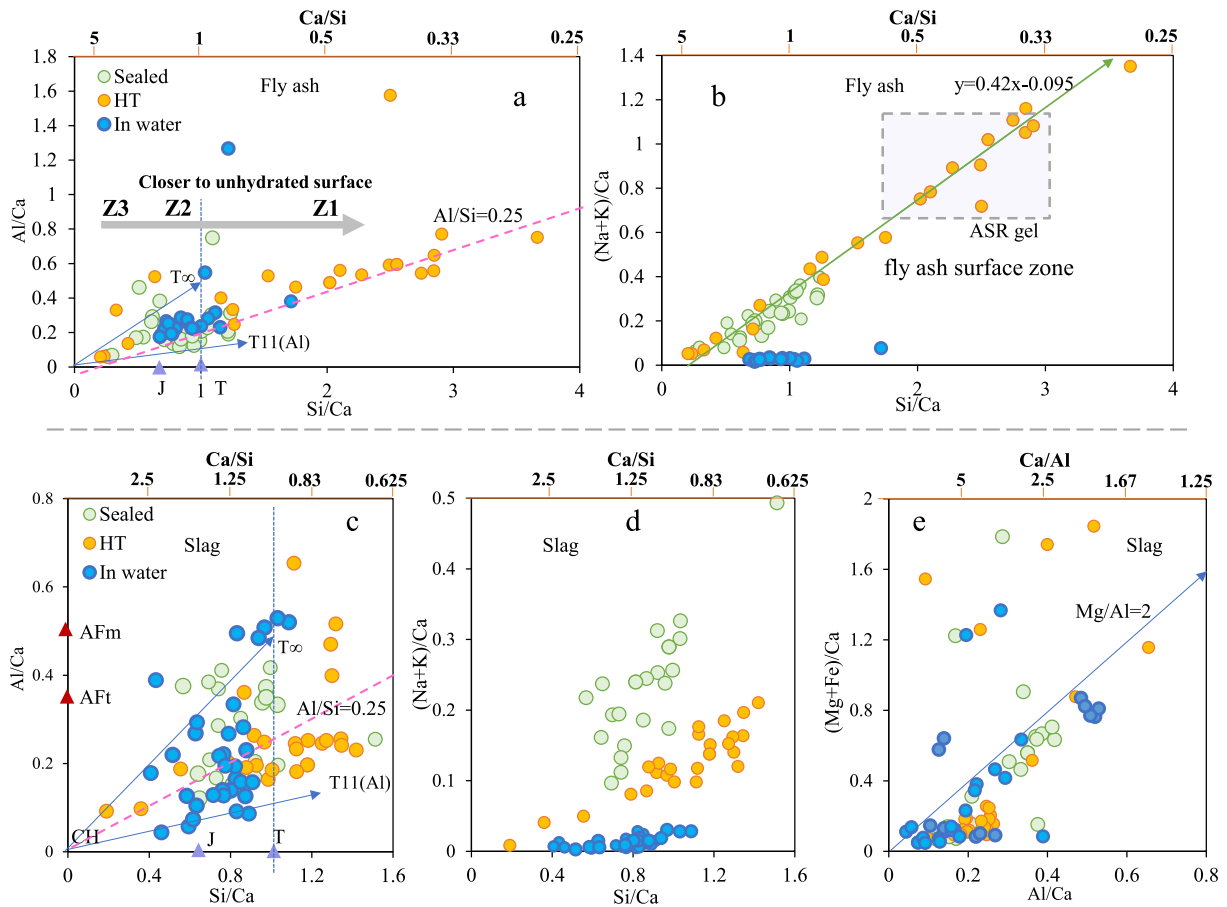
Fig. 9. Statistics of EDS data from local zone near the fly ash and slag particles: tobermorite (T), jennite (J).

formation of additional hydrotalcite phase and C-A-S-H. Like fly ash samples, the (Na + K)/Ca ratio in the water-cured slag samples is extremely low. As shown in Fig. 9e, the Mg/Al ratio in the inner hydration products is either equal to or lower than the minimum probable value for hydrotalcite-like phases, typically around 2 [93]. Hydrotalcite itself has a Mg/Al ratio of 3 ($[Mg_6Al_2(OH)_{16}]CO_3 \cdot 4H_2O$). One of the plausible explanation for this is the presence of interstratified layers of $Al(OH)_3$ structures within the Mg—Al double hydroxide layers. Additionally, the presence of C-A-S-H mixed with the inner hydration products could contribute to reduction in the Mg/Al and Al/Ca ratios.

4. General discussion

Later-age hydration is limited by the availability of water under sealed conditions, as hydration products can only form in water-filled spaces. Self-desiccation in the sealed blends significantly slows down hydration by reducing the volume of water-filled pores available for further reactions, particularly at later ages [14,16]. Fig. 10 shows the internal RH of sealed pastes after 600 d curing. Under room temperature curing, the internal RH of fly ash and slag blends reaches 85.5% (±4) and 86.7% (±3.2), respectively. After 390 days at elevated temperatures, the internal RH drops to 79.1% (±2.9) for the fly ash blends and 76.5% (±2.5) for the slag blends, indicating further water depletion due to activated later-age hydration. Using the Kelvin equation with ionic effects [19], liquid water in the fly ash blends is confined to pores smaller than 16.6 nm, and for slag blends, to pores smaller than 19.3 nm. Elevated temperatures appear to deplete water from pores ranging between 10.5 and 16.6 nm in the fly ash blends, and between 9.1 and 19.3 nm in the slag blends. This suggests that the limited availability of liquid water in nanopores determines hydration reactions at the later stage.
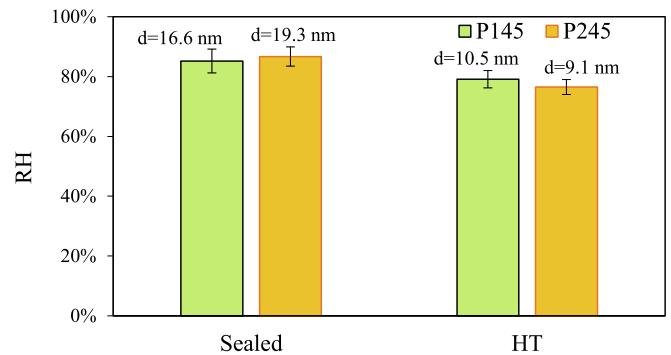

Fig. 10. Equilibrated RH of crushed pastes.

In addition to the limited availability of water in sealed curing, the rate of hydration is also constrained by other factors, even when moisture is sufficient. For example, it has been shown that the hydration of belite (a major phase in Portland cement) in blended systems can approach near-complete hydration after one year, but only under elevated temperatures (30–60 °C) [29]. This is consistent with findings from this study, where the fly ash and slag pastes, even under water curing until 600 days, remained a significant portion of unhydrated (see Fig. 2 and Fig. 8). Furthermore, a substantial amount of portlandite is unconsumed in both systems, suggesting that even under saturated conditions, there are kinetic barriers to complete hydration.

The thermodynamic and kinetic behavior of hydration reactions in these confined spaces is critical to understanding the later-age hydration mechanisms. The confined pore environment, combined with a reduced

volume of pore solution, alters the dissolution and precipitation processes, thereby slowing hydration kinetics. Therefore, the key to understanding later-age hydration lies in unraveling how confinement impacts the thermodynamics and kinetics of hydration reaction within these nanopore spaces.

4.1. Thermodynamics of continuous hydration in pores

4.1.1. Dissolution confined in pores

As shown Figs. 2, 7 and 8, belite and minerals in SCMs remain unhydrated after a long-term curing (e.g. one year). To understand the dissolution kinetics of these materials, we use the dissolution of belite as an example:

$$Ca_2SiO_4 + 4H_2O = 2Ca^{2+} + 4OH^- + H_4SiO_4$$
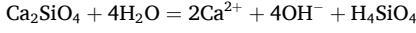
The dissolution reaction of belite is thermodynamically governed by the saturation degree of the bulk solution, which can be calculated with Eq. (1) [28].

$$S_{d\infty} = ln\frac{Q}{K(P_0)} = ln\left(a_{Ca^{2+}}^2 \times a_{OH^-}^4 \times a_{H_4SiO_4}^2\right) - 4lna_{H_2O(\infty)} - lnK(P_0) \quad (1)$$

where $S_{d\infty}$ is the saturation index of bulk solution (without any confinement) with respect to belite dissolution, Q is the ion activity product, $K(P_0)$ is the equilibrium constant at the reference pressure P_0, a_i represents the activities of ion species and $a_{H_2O(\infty)}$ is water activity in bulk solution.

In the unsaturated porous material with a hydrophilic pore wall, capillary pressure plays a critical role, influenced by the curvature of the pore walls. Using the Young-Laplace law and Kelvin equation, we can express the impact of pore size on water activity and capillary pressure, as shown in Eq. (2), with an assumption of cylindrical pore shape.

$$ln\frac{a_{H_2O(r)}}{a_{H_2O(\infty)}} = \frac{V_s}{RT}\Delta P = -\frac{2\sigma_{s,v}V_s}{RT} \times \frac{1}{r} \quad (2)$$

where $a_{H_2O(r)}$ is the water activity in cylindrical pore with radius of r, V_S is the molar volume of solution, $\sigma_{s,v}$ is the interfacial energy between the liquid and vapor (7.28×10^{-2} J/m² for water at 20 °C), R is the universal gas constant and T is the temperature.

Moreover, this confinement alters the equilibrium constant for dissolution, which can be adjusted for pore pressure using Eq. (3) [94,95]:

$$\frac{\partial(lnK)}{\partial P} = -\frac{\Delta V}{RT} \quad (3)$$

where ΔV is difference between the partial molar volume of electrolyte at the concentrated and infinitely diluted condition. Assuming that it is independent on the pressure change, the solution of Eq. (3) can be obtained as [96]:

$$ln\frac{K(P_r)}{K(P_0)} = \frac{\Delta V\sigma_{s,v}}{RT} \times \frac{1}{r} \quad (4)$$

where $K(P_r)$ is the equilibrium constant at pressure P_r in the cylindrical pore. Substituting Eq. (2) and (4) into Eq. (1), the effect of pore size on the dissolution under confinement can be written as Eq. (5) and simplified as Eq. (6) with respect to saturation index in bulk solution.

$$\begin{aligned} S_{dr} = ln\frac{Q}{K(P_r)} &= ln\left(a_{Ca^{2+}}^2 \times a_{OH^-}^4 \times a_{H_4SiO_4}^2\right) - 4lna_{H_2O(r)} - lnK(P_r) \\ &= ln\left(a_{Ca^{2+}}^2 \times a_{OH^-}^4 \times a_{H_4SiO_4}^2\right) \\ &\quad - 4\left(lna_{H_2O(\infty)} - \frac{2\sigma_{s,v}V_s}{RT} \times \frac{1}{r}\right) - lnK(P_0) + \frac{2\sigma_{s,v}\Delta V}{RT} \end{aligned} \quad (5)$$

$$S_{dr} = S_{d\infty} + (4V_s - \Delta V)\frac{2\sigma_{s,v}}{RT} \times \frac{1}{r} \quad (6)$$

where S_{dr} is the saturation index with respect to dissolution of belite in pores with the diameter of r.

4.1.2. Nucleation confined in pores

Nucleation will occur while the concentration of ions reaches the supersaturation state of hydration products. Nucleation is similarly affected by confinement. C-S-H is the major product for Porland cement-based system. To simplify the analysis, we used reaction of torbermorite [46] as below to reveal the effect of confinement on thermodynamics of precipitation.

$$Ca^{2+} + 2OH^- + 1.5H_4SiO_4 = CaO \cdot 1.5(SiO_2) \cdot 2.5H_2O + 1.5H_2O$$
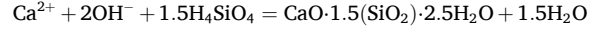
The nucleation of these phases is governed by the saturation state, and the saturation index for nucleation of torbermorite in bulk solution ($S_{p\infty}$) can be written as Eq. (7).

$$S_{p\infty} = 1.5lna_{H_2O(\infty)} - ln\left(a_{Ca^{2+}} \times a_{OH^-}^2 \times a_{H_4SiO_4}^{1.5}\right) - lnK_t(P_0) \quad (7)$$

where $K_t(P_0)$ is the equilibrium constant with respect to the nucleation of torbermorite at pressure P_0. With consideration of confinement effect on water activity by Eq. (2) and equilibrium constant by Eq. (4), the saturation index in pores (S_{pr}) reads Eq. (8).

$$S_{pr} = S_{p\infty} - (1.5V_s + \Delta V)\frac{2\sigma_{s,v}}{RT} \times \frac{1}{r} \quad (8)$$

4.1.3. Effect of ion concentration and pore size on hydration

The ionic concentration in pore solutions also affects hydration by altering water activity and molar volume, described by the Raoult's law [97,98] as follow:

$$RH_s = \frac{a'_{H_2O(\infty)}}{a_{H_2O(\infty)}} = \frac{n_w}{n_w + n_i} \quad (9)$$

where RHs is the relative humidity for liquid-vapor transition in electrolyte, $a'_{H_2O(\infty)}$ is the water activity in electrolyte, $a_{H_2O(\infty)}$ is the activity of pure water, n_w is the moles of water in the solution and n_i is the total moles of ions in the solution. Ions in solution also change the molar volumes of electrolyte, and this effect can be estimated with Eq. (10) and (11) [99]:

$$\Delta V = k_c\sqrt{C} \quad (10)$$

$$V_s = V_0 + k_c\sqrt{C} \quad (11)$$

where k_c is the slope for concentration dependence (1.78 at 20 °C), C is the total molar concentration of ions, and V_0 is the molar volume of water (18 cm³/mol at 20 °C).

According to a review for concentration data of extracted pore solution, the main ions in pore solution comprise Na⁺, K⁺, OH⁻, and Ca²⁺ [100]. To consider the effect of ions on the water activity and molar volume, a typical total molar concentration of 0.4 mol/L is used for bulk later-age pore solution, which results in a RHs of 98%. In scenarios with elevated alkalinity, the total molar concentration is assumed to be 4 mol/L, resulting in an RHs of 83%. The saturation index for belite dissolution remains near 0 in bulk solutions, while the index for C-S-H precipitation is approximately 0.5 under these conditions [26]. Table 4 summarizes the value of relevant parameters used in the modelling.

In light of the thermodynamic model applied, we can use Eqs. (6) and (8) to estimate the effects of pore size and ionic concentration on the saturation indices for both dissolution and precipitation, as illustrated in Fig. 11. The reduction in pore size results in an increase of saturation index for dissolution, indicating that mineral dissolution in confined pores is suppressed. Conversely, increased alkalinity lowers the saturation index, thereby promoting dissolution. However, a decrease in pore sizes reduces the saturation index for nucleation of tobermorite. The

Table 4

Value of constant parameters used in the modelling adopted from relevant publications.

Parameter	Symbol	Value
Saturation index for dissolution in bulk	S_d	0
Saturation index for nucleation in bulk	S_p	0.5
Molar volume of water at 20 °C	V_S (cm^3/mol)	18
Surface tension at 20 °C	$\sigma_{s,v}$ (J/m^2)	7.28×10^{-2}
Total ion concentration	C (mol/L)	0.4 for water cuing, 4 for sealed curing
Molar concentration slope	k_c	1.78

calculations reveal that when liquid water is confined to pores with diameters smaller than approximately 3.6 nm, corresponding to a critical relative humidity (RH) of 76%, the saturation index falls below zero. This suggests that under these conditions tobermorite are unable to nucleate.

Moreover, a higher alkalinity raises the critical RH required for nucleation, further inhibiting the process in confined pores. Elevated temperatures, on the other hand, can lower the critical RH to about 70% for pore solutions with a molar concentration of 0.4 M, allowing for some level of hydration even in restricted spaces. The identified critical RH for nucleation is close to previous experimental investigations [21,22]. These findings align with the experimental data (Figs. 2–3), where elevated later-age curing temperatures result in only marginal increases in the degree of hydration, despite further reducing the internal RH (as seen in Fig. 10). The results confirm that later-age hydration is predominantly limited by nucleation processes in confined pores.

4.2. Kinetics of crystallization confined in pore space

The previous section identifies the thermodynamic limits for hydration in samples under unsaturated curing conditions, which suggests that the hydration rate at later-age is determined by nucleation kinetics, and it will stop due to the reduced water availability. The initial step in the precipitation of primary flocs of hydration products can be described by classical nucleation theory. The homogeneous nucleation rate (J) for liquid–solid systems follows the Arrhenius reaction rate equation [101,102], expressed as:

$$J = J_n e^{-\Delta G_{crit}/k_B T} \tag{12}$$

where ΔG_{crit} is the thermodynamic barrier for forming a critical molecular cluster, k_B is the Boltzmann constant, and J_n is a pre-exponential factor that serves as a kinetic constant. For spherical clusters, the thermodynamic barrier is given by Eq. (13) [103].

$$\Delta G_{crit} = \frac{16\pi\sigma^3 v^2}{3(k_B T S)^2} \tag{13}$$

where σ is interfacial tension, S is the supersaturation index, and v is the molar volume of the cluster.

To consider effects of confinement, we evaluate the nucleation rate in pores (J_r) by referring to the rate in bulk solution (J_∞) at the same ion concentration. The relative nucleation rate can be calculated by Eq. (14):

$$\ln\frac{J_r}{J_\infty} = \frac{16\pi\sigma^3 v^2}{3(k_B T)^3} \times \left(\frac{1}{S_{p\infty}^2} - \frac{1}{S_{pr}^2} \right) \tag{14}$$

The value of $\frac{16\pi\sigma^3 v^2}{3(k_B T)^3}$ for nucleation of the synthetic C-S-H is approximately 32 at room temperature [102]. By substituting this parameter into Eqs. (8) and (14), we can estimate the effect of confinement, temperature, and alkalinity on the nucleation kinetic in small pores.

Fig. 12 shows that increasing the alkalinity (e.g. ion concentration from 0.4 to 4 M) strongly suppresses the nucleation rate of torbermorite in pores. Additionally, moisture deficiency in larger pores considerably slows down the nucleation process. For instance, reducing the available water from a pore radius of 100 nm to 50 nm results in a decrease in the nucleation rate by a factor of 1×10^7. Conversely, raising the curing temperature increases the solution's saturation degree, directly accelerating the nucleation rate.

The induction period is defined as the time required for the appearance of the first super nucleus in the solution, marking the point
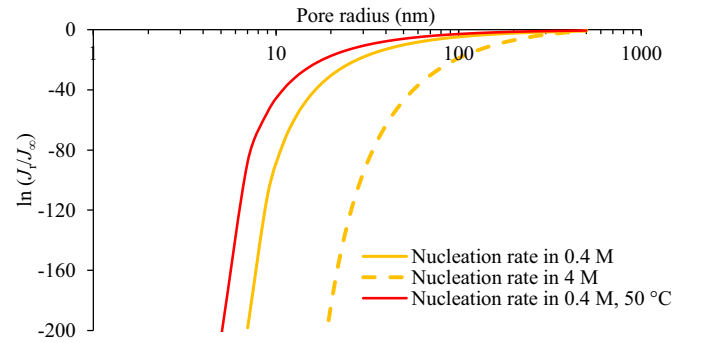
Fig. 12. Relative nucleation rate of calcium silicate hydrate in the pores with respect to the pore radius.
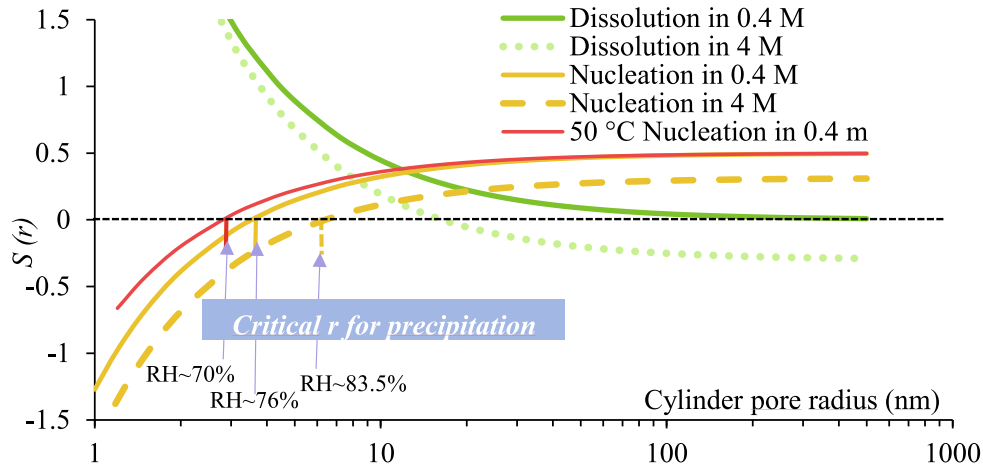
Fig. 11. Saturation state of the confined pore solution with respect to dissolution of belite and precipitation of calcium silicate hydrate, assuming a total ion concentration of 0.4 and 4 mol/L.

at which the solution breaks its metastable state. Assuming stationary nucleation and a super nucleus with N units, induction period (t_i) for precipitation in confined pore space (V) is given by [104,105].

$$t_i = N/JV \tag{15}$$

Therefore, even when sufficient moisture is available, for instance water curing, the precipitation of hydration products in small nanopores occurs at a much slower rate compared to capillary pore solution. Given similar degrees of saturation, the precipitation rate on sample's surface is significantly faster than in inner hydration products within much smaller gel pores. As a result, concentrated ions from the dissolving front of unhydrated minerals (characterized by a dense structure [35,36]) gradually transport to the outer product and eventually to the surface of the samples (particles), where more space is available for nucleation and growth. However, this process involves the diffusion of ions from the inner front to the larger pores, which rate can be one of the controlling factors for hydration in saturated samples.

4.3. Effect of curing regimes on later-age hydration and microstructure

4.3.1. Sealed curing

Sealed curing can cause the internal RH of blended paste to drop below 95% after two weeks [17]. Even with a high w/b ratio, self-desiccation significantly reduces RH, particularly in systems blended with blast-furnace slag [18]. As illustrated in Fig. 14, this reduced RH limits the liquid water being only accessible in small nanopore spaces to decrease water activity. As size of pores containing liquid water decreases (Fig. 12), the nucleation rate of hydration products is greatly decreased. Although elevated curing temperatures enhance early hydration, after 390 days, there is only a marginal improvement in the later-age hydration of fly ash and slag under sealed curing (Figs. 2 and

3). This results in a minor decrease in the volume of big capillary pores (Fig. 4), with a corresponding increase in gel pores (Fig. 5). While higher temperatures accelerate nucleation within confined pore spaces, a lack of liquid water in sealed samples limits the hydration only occurring with RH higher than 70% (Fig. 11). This explains the small difference in internal RH observed between samples cured at room temperature and those exposed to elevated temperatures (Fig. 10).

Additionally, increased temperatures cause water redistribution in hydration products [83], which leads to the migration of water from gel pores into capillary pores. Consequently, later-age hydration occurs in the larger pores, resulting in a slightly refined pore structure (Figs. 7 and 8) and a reduction in interlayer water (Fig. 6). The enhanced hydration by temperature results in a lower Q1 and higher Q2b in silicate chains, thereby increasing the mean chain length (Fig. 3). As shown in Fig. 13, for slag-blended pastes, elevated temperature seems to stabilize C-S-H with a lower Ca/Si ratio (such as CSHQ-TobD and CSHQ-TobH). However, types of C-S-H in fly ash blends remain rather stable across different temperatures. Therefore, we can conclude that changes of silicate chain in fly ash pastes at elevated temperature are mainly ascribed to the enhanced hydration degree. The elevated temperature causes a (K + Na)/Ca ratio > 0.4 in local products of fly ash, which is much higher than typical alkali uptake in C-A-S-H with a value lower than 0.15 [106,107]. The much higher alkali content may result from the accumulation of alkali ions in the limited volume of pore solution near the unhydrated surface. Temperature also affects ion concentrations and pH in the paste [108], factors which are not considered in this study. This limitation of current work underscores the need for further investigation for better understanding of these processes.

4.3.2. Water curing

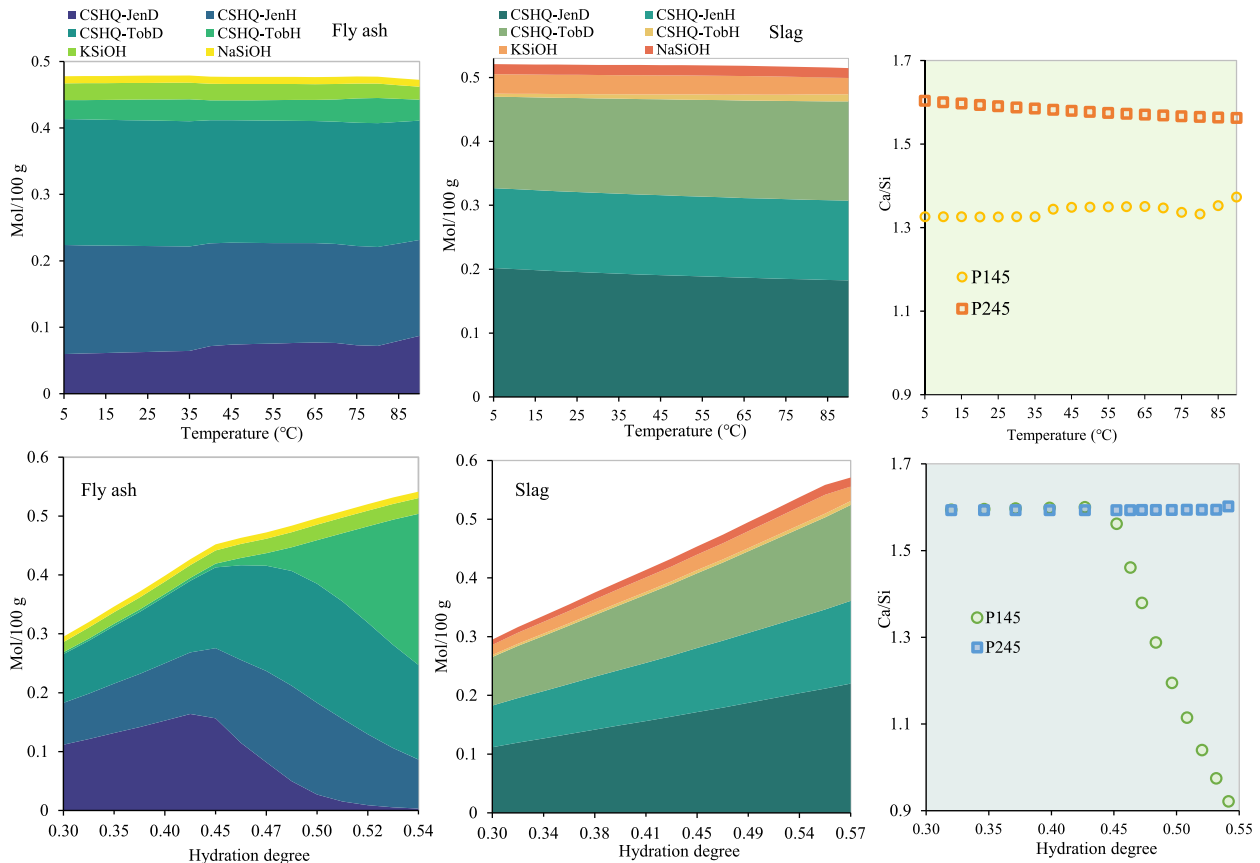Water curing since 7 d largely enhances the hydration degree of fly

Fig. 13. Thermodynamic modelling of C-S-H phase in hydration products: effect of temperature assuming hydration degree of SCMs as 60%; and effects of hydration degree of SCMs at 20 °C.

ash (Fig. 3), which in turn results in the consumption of portlandite (Fig. 2) and a markedly lower Ca/Si ratio in C-A-S-H structure (Fig. 7). Thermodynamic modelling proves that as the hydration degree of fly ash increases, more C-A-S-H forms, and the Ca/Si ratio decreases significantly, particularly when the hydration degree exceeds ~0.42 (Fig. 13). In contrast, the enhanced hydration of slag under water curing has a limited effect on the Ca/Si ratio of local hydration products (Fig. 9), which is somehow consistent with the thermodynamic modelling results. However, it is important to note that the current thermodynamic modelling does not comprehensively account for the behavior ions adsorption and aluminum in C-A-S-H. Water curing in this study also leads to a general increase in the volume of pores across all size ranges. As shown in Figs. 7 and 8, later-stage water curing promotes the precipitation of hydration products on the surface of the samples, connecting the smaller particles to form a large volume of new capillary pores. The enhanced hydration increases C-A-S-H content, which in turn increases the volume of interlayer and gel pores (Figs. 4–6). Water curing induces a notable reduction of Na and K in the local products near the fly ash or slag grains (Fig. 9). The reduced local alkali concentrates can contribute to acceleration of nucleation (Fig. 11).

As demonstrated by Fig. 14, despite sufficient water, hydration within extremely confined spaces can be significantly inhibited. Previous studies have shown that confinement can stabilize intermediate amorphous phases, such as amorphous calcium carbonates, during the crystallization within pores [109]. A similar process likely occurs during the precipitation of C-A-S-H, where the stabilization of primary flocs (with a size around few nanometers [110,111]) suppresses the second step of nucleation, thus arresting C-A-S-H growth. The features of inner and outer products cause differences in nucleation rate. Nucleation occurs more slowly in the inner zones due to spatial confinement, resulting in higher local supersaturation and ion concentrations. This, in turn, creates a concentration gradient, driving ion migration from the unhydrated surface outward. Therefore, ions tend to move toward outer or bulk zones, where coarser pores allow faster nucleation rates. On water-covered surfaces, there is sufficient space for nucleation to form a surface layer, leading to an overall increase in total pore volume. The stabilization of Mc and Hc in the surface zone is probably due to the migration and leaching of K and Na to the particle surfaces (Figs. 2 and 7).

Unlike sealed curing, where limited water availability is the primary factor that slows later-age hydration. Water curing can change the later-age hydration in three ways: (1) it maintains thermodynamic conditions for precipitation, (2) it provides channels for migration of ions from dissolving front to larger pores or particle surfaces, thus accelerating hydration, and (3) it facilitates the leaching of alkali ions, which lowers local concentrations and thus promotes a faster nucleation.

Nevertheless, it remains unclear about the relative importance of ion migration versus nucleation within nanopores as the primary rate-controlling mechanism for later-age hydration in blended binders. Further detailed investigation is required to better understand the governing processes under water curing conditions.

5. Concluding remarks

A clear understanding of later-age hydration is essential for optimizing the use of both cement and SCMs in sustainable concretes. In this study, a comprehensive investigation was conducted to quantify the influence of extended curing regimes on the microstructure and composition of pastes blended with fly ash and slag. The key findings can be summarized as follows:

After 600 d of sealed curing, most of the alite and aluminate in blended pastes are consumed, while some belite and a significant portion of fly ash and slag remain unreacted. Elevated temperature applied after 390 d slightly enhances later-age hydration by activating local reactions near the fly ash and slag grains. However, the lack of sufficient water limits this effect, leading to a moderate reduction in the content of Mc but a noticeable reduction in portlandite of fly ash blends. In contrast, the portlandite content in slag blends shows little increase at elevated temperature. Moreover, increasing the curing temperature slightly reduces the volume of large capillary pores, though it also reduces moisture in the interlayer of C-A-S-H due to moisture redistribution. Temperature has a stronger effect on microstructure of slag blends compared to fly ash under sealed curing. This results in a larger increase in gel pore volume, more pronounced change in the Si/Ca ratio near
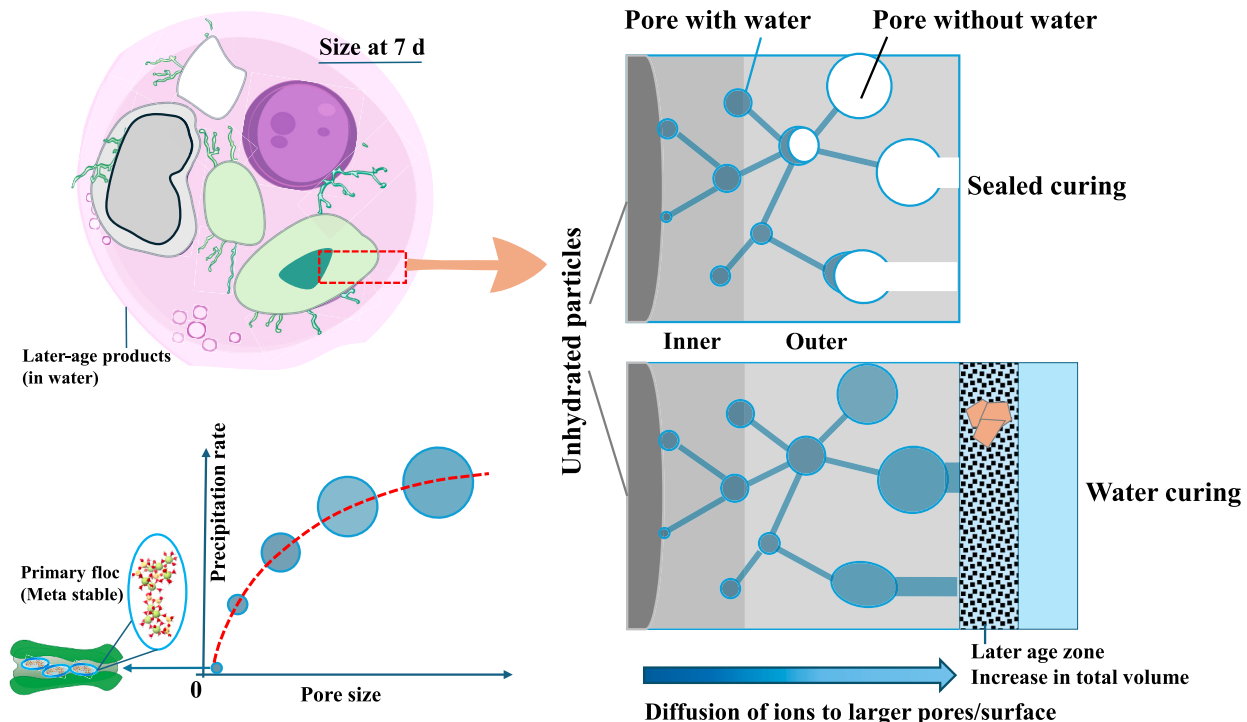

Fig. 14. Illustration of later-age hydration mechanisms.

unhydrated surface, and a larger reduction in the internal RH after elevated temperature curing.

Water Curing applied after 7 d significantly accelerates the hydration of belite, fly ash, and slag. This results in a significant reduction in portlandite content in blended pastes and an increase in bound water associated with C-A-S-H and calcium aluminate hydrates (ettringite, Mc, and Hc). Water curing also promotes the formation of later-age hydration products on the particle surfaces, where Mc and Hc are stably precipitated with a higher content compared to that in sealed samples. Furthermore, water curing increases the total volume of pores across all sizes due to migration and leaching of ions to particle surfaces, which facilitates later-age hydration. C-A-S-H in water-cured samples has a longer mean chain length and much lower alkali uptake.

Insights into later-age under different curing regimes are provided from thermodynamic and kinetic modelling of dissolution and precipitation. The limited availability of water in sealed conditions significantly alters the thermodynamic state of the pore solution, slowing and even stopping the nucleation of hydration products. The estimated RH limits for later-age hydration closely match experimental findings of sealed samples, indicating that later-age hydration of sealed samples is primarily governed by kinetics of nucleation. Elevated temperature curing increases the saturation index of pore solutions, enhancing nucleation kinetics and promoting later-age hydration.

Water curing provides sufficient moisture for dissolution and precipitation. However, the limited pore space near the unhydrated surface restricts the nucleation rate so it slows the later-age hydration. Given the same saturation state, nucleation in outer products and surface zones is much faster than inner zones. Water curing provides channels for migration of ions from dissolving front to larger pores or particle surfaces to accelerate hydration. For later-age reaction in water-curing samples, whether ion migration or nucleation within nanopores is the rate-controlling step requires further experimental and modelling investigations.

CRediT authorship contribution statement

Liming Huang: Writing – review & editing, Writing – original draft, Visualization, Validation, Software, Resources, Methodology, Investigation, Formal analysis, Data curation, Conceptualization. **Luping Tang:** Writing – review & editing, Writing – original draft, Supervision, Project administration, Funding acquisition. **Zhijun Dong:** Writing – review & editing, Resources, Methodology. **Birhan Alkadir Abdulahi:** Writing – review & editing, Formal analysis, Data curation. **Zhenghong Yang:** Writing – review & editing, Supervision, Project administration.

Declaration of competing interest

We declare that there are no known competing financial interests or personal relationships that could have appeared to influence the work reported in this paper.

Acknowledgements

Appendix A. Supplementary data

Supplementary data to this article can be found online at https://doi. org/10.1016/j.cemconres.2025.107785.

Data availability

Data will be made available on request.

References

[1] K.L. Scrivener, V.M. John, E.M. Gartner, Eco-efficient cements: potential economically viable solutions for a low-CO2 cement-based materials industry, Cem. Concr. Res. 114 (2018) 2–26, https://doi.org/10.1016/j.cemconres.2018.03.015.

[2] R. Snellings, P. Suraneni, J. Skibsted, Future and emerging supplementary cementitious materials, Cem. Concr. Res. 171 (2023) 107199, https://doi.org/10.1016/j.cemconres.2023.107199.

[3] B. Lothenbach, K. Scrivener, R.D. Hooton, Supplementary cementitious materials, Cem. Concr. Res. 41 (2011) 1244–1256, https://doi.org/10.1016/j.cemconres.2010.12.001.

[4] K.L. Scrivener, B. Lothenbach, N. De Belie, E. Gruyaert, J. Skibsted, R. Snellings, A. Vollpracht, TC 238-SCM: hydration and microstructure of concrete with SCMs, Mater. Struct. 48 (2015) 835–862.

[5] L. Huang, L. Tang, I. Löfgren, N. Olsson, Z. Yang, Real-time monitoring the electrical properties of pastes to map the hydration induced microstructure change in cement-based materials, Cem. Concr. Compos. 132 (2022) 104639, https://doi.org/10.1016/j.cemconcomp.2022.104639.

[6] L. Huang, L. Tang, I. Löfgren, N. Olsson, Z. Yang, Y. Li, Moisture and ion transport properties in blended pastes and their relation to the refined pore structure, Cem. Concr. Res. 161 (2022) 106949, https://doi.org/10.1016/j.cemconres.2022.106949.

[7] L. Huang, L. Tang, I. Löfgren, N. Olsson, A. Babaahmadi, O. Esping, Y. Li, Z. Yang, Non-destructive test system to monitor hydration and strength development of low CO2 concrete, Constr. Build. Mater. 408 (2023) 133774, https://doi.org/10.1016/j.conbuildmat.2023.133774.

[8] K. De Weerdt, M.B. Haha, G. Le Saout, K.O. Kjellsen, H. Justnes, B. Lothenbach, Hydration mechanisms of ternary Portland cements containing limestone powder and fly ash, Cem. Concr. Res. 41 (2011) 279–291.

[9] V. Kocaba, E. Gallucci, K.L. Scrivener, Methods for determination of degree of reaction of slag in blended cement pastes, Cem. Concr. Res. 42 (2012) 511–525.

[10] J.I. Escalante, L.Y. Gomez, K.K. Johal, G. Mendoza, H. Mancha, J. Mendez, Reactivity of blast-furnace slag in Portland cement blends hydrated under different conditions, Cem. Concr. Res. 31 (2001) 1403–1409.

[11] J.I. Escalante-Garcia, J.H. Sharp, Effect of temperature on the hydration of the main clinker phases in Portland cements: part I, neat cements, Cem. Concr. Res. 28 (1998) 1245–1257.

[12] E. Sakai, S. Miyahara, S. Ohsawa, S.-H. Lee, M. Daimon, Hydration of fly ash cement, Cem. Concr. Res. 35 (2005) 1135–1140, https://doi.org/10.1016/j.cemconres.2004.09.008.

[13] T.C. Powers, T.L. Brownyard, Studies of the physical properties of hardened Portland cement paste, in: Journal Proceedings, 1946, pp. 101–132.

[14] T.C. Powers, A Discussion of Cement Hydration in Relation to the Curing of Concrete, Portland Cement Association, 1947.

[15] O.M. Jensen, P.F. Hansen, Water-entrained cement-based materials I. Principles and theoretical background, Cem. Concr. Res. 34 (2001) 647–654.

[16] M. Wyrzykowski, P. Lura, Effect of relative humidity decrease due to self-desiccation on the hydration kinetics of cement, Cem. Concr. Res. 85 (2016) 75–81, https://doi.org/10.1016/j.cemconres.2016.04.003.

[17] M. Pathirage, D.P. Bentz, G. Di Luzio, E. Masoero, G. Cusatis, The ONIX model: a parameter-free multiscale framework for the prediction of self-desiccation in concrete, Cem. Concr. Compos. 103 (2019) 36–48, https://doi.org/10.1016/j.cemconcomp.2019.04.011.

[18] Y. Briki, M. Zajac, M.B. Haha, K. Scrivener, Factors affecting the reactivity of slag at early and late ages, Cem. Concr. Res. 150 (2021) 106604, https://doi.org/10.1016/j.cemconres.2021.106604.

[19] L. Huang, L. Tang, L. Wadsö, I. Löfgren, N. Olsson, Z. Yang, Using water vapour and N2 isotherms to unveil effects of SCMs on nanopores and evaluate hydration degree, Cem. Concr. Res. 164 (2023) 107042.

[20] F. Zunino, K. Scrivener, Microstructural developments of limestone calcined clay cement (LC3) pastes after long-term (3 years) hydration, Cem. Concr. Res. 153 (2022) 106693, https://doi.org/10.1016/j.cemconres.2021.106693.

[21] O.M. Jensen, P.F. Hansen, E.E. Lachowski, F.P. Glasser, Clinker mineral hydration at reduced relative humidities, Cem. Concr. Res. 29 (1999) 1505–1512, https://doi.org/10.1016/S0008-8846(99)00132-5.

[22] R.J. Flatt, G.W. Scherer, J.W. Bullard, Why alite stops hydrating below 80% relative humidity, Cem. Concr. Res. 41 (2011) 987–992, https://doi.org/10.1016/j.cemconres.2011.06.001.

[23] Q. Jiang, M.D. Ward, Crystallization under nanoscale confinement, Chem. Soc. Rev. 43 (2014) 2066–2079, https://doi.org/10.1039/C3CS60234F.

[24] D. Kim, B. Lee, S. Thomopoulos, Y.-S. Jun, The role of confined collagen geometry in decreasing nucleation energy barriers to intrafibrillar mineralization, Nat. Commun. 9 (2018) 962, https://doi.org/10.1038/s41467-018-03041-1.

[25] A.J. Page, R.P. Sear, Heterogeneous nucleation in and out of pores, Phys. Rev. Lett. 97 (2006) 065701, https://doi.org/10.1103/PhysRevLett.97.065701.

[26] M. Zajac, J. Skocek, B. Lothenbach, B.H. Mohsen, Late hydration kinetics: indications from thermodynamic analysis of pore solution data, Cem. Concr. Res. 129 (2020) 105975, https://doi.org/10.1016/j.cemconres.2020.105975.

[27] A. Putnis, M. Prieto, L. Fernandez-Diaz, Fluid supersaturation and crystallization in porous media, Geol. Mag. 132 (1995) 1–13, https://doi.org/10.1017/S0016756800011389.

[28] D. Benavente, Role of pore structure in salt crystallisation in unsaturated porous stone, J. Cryst. Growth 260 (2004) 532–544, https://doi.org/10.1016/j.jcrysgro.2003.09.004.

[29] J.I. Escalante-Garcıa, J.H. Sharp, Effect of temperature on the hydration of the main clinker phases in Portland cements: part II, blended cements, Cem. Concr. Res. 28 (1998) 1259–1274.

[30] R. Snellings, A. Machner, G. Bolte, H. Kamyab, P. Durdzinski, P. Teck, M. Zajac, A. Muller, K. De Weerdt, M.B. Haha, Hydration kinetics of ternary slag-limestone cements: impact of water to binder ratio and curing temperature, Cem. Concr. Res. 151 (2022) 106647, https://doi.org/10.1016/j.cemconres.2021.106647.

[31] B. Lothenbach, F. Winnefeld, C. Alder, E. Wieland, P. Lunk, Effect of temperature on the pore solution, microstructure and hydration products of Portland cement pastes, Cem. Concr. Res. 37 (2007) 483–491, https://doi.org/10.1016/j.cemconres.2006.11.016.

[32] K. De Weerdt, M. Ben Haha, G. Le Saout, K.O. Kjellsen, H. Justnes, B. Lothenbach, The effect of temperature on the hydration of composite cements containing limestone powder and fly ash, Mater. Struct. 45 (2012) 1101–1114, https://doi.org/10.1617/s11527-011-9819-5.

[33] E. Berodier, K. Scrivener, Evolution of pore structure in blended systems, Cem. Concr. Res. 73 (2015) 25–35.

[34] F. Avet, K. Scrivener, Investigation of the calcined kaolinite content on the hydration of limestone calcined clay cement (LC3), Cem. Concr. Res. 107 (2018) 124–135.

[35] M.J. DeJong, F.-J. Ulm, The nanogranular behavior of C-S-H at elevated temperatures (up to 700 °C), Cem. Concr. Res. 37 (2007) 1–12, https://doi.org/10.1016/j.cemconres.2006.09.006.

[36] M. Sebastiani, R. Moscatelli, F. Ridi, P. Baglioni, F. Carassiti, High-resolution high-speed nanoindentation mapping of cement pastes: unravelling the effect of microstructure on the mechanical properties of hydrated phases, Mater. Des. 9 (2016).

[37] B. Li, Q. Li, W. Chen, Spatial zonation of a hydrotalcite-like phase in the inner product of slag: new insights into the hydration mechanism, Cem. Concr. Res. 145 (2021) 106460, https://doi.org/10.1016/j.cemconres.2021.106460.

[38] R. San Nicolas, S.A. Bernal, R.M. de Gutiérrez, J.S. van Deventer, J.L. Provis, Distinctive microstructural features of aged sodium silicate-activated slag concretes, Cem. Concr. Res. 65 (2014) 41–51.

[39] J.W. Bullard, H.M. Jennings, R.A. Livingston, A. Nonat, G.W. Scherer, J. S. Schweitzer, K.L. Scrivener, J.J. Thomas, Mechanisms of cement hydration, Cem. Concr. Res. 41 (2011) 1208–1223, https://doi.org/10.1016/j.cemconres.2010.09.011.

[40] K. Scrivener, A. Ouzia, P. Juilland, A. Kunhi Mohamed, Advances in understanding cement hydration mechanisms, Cem. Concr. Res. 124 (2019) 105823, https://doi.org/10.1016/j.cemconres.2019.105823.

[41] L. Huang, Water and Alkali Salts in the Hydrating and Hardened Green Cement-based Materials: Hydration Process, Moisture Content and Transport, Licentiate thesis,, Chalmers Tekniska Hogskola (Sweden), 2022.

[42] R. Snellings, J. Chwast, Ö. Cizer, N. De Belie, Y. Dhandapani, P. Durdzinski, J. Elsen, J. Haufe, D. Hooton, C. Patapy, RILEM TC-238 SCM recommendation on hydration stoppage by solvent exchange for the study of hydrate assemblages, Mater. Struct. 51 (2018) 1–4.

[43] K. Scrivener, R. Snellings, B. Lothenbach, A Practical Guide to Microstructural Analysis of Cementitious Materials, Crc Press, 2018.

[44] S. Diamond, Mercury porosimetry an inappropriate method for the measurement of pore size distributions in cement-based materials, Cem. Concr. Res. 30 (2000).

[45] L.B. Rockland, Saturated salt solutions for static control of relative humidity between 5° and 40° C, Anal. Chem. 32 (1960) 1375–1376, https://doi.org/10.1021/ac60166a055.

[46] B. Lothenbach, D.A. Kulik, T. Matschei, M. Balonis, L. Baquerizo, B. Dilnesa, G. D. Miron, R.J. Myers, Cemdata18: a chemical thermodynamic database for hydrated Portland cements and alkali-activated materials, Cem. Concr. Res. 115 (2019) 472–506, https://doi.org/10.1016/j.cemconres.2018.04.018.

[47] T. Thoenen, W. Hummel, U. Berner, E. Curti, The PSI/Nagra Chemical Thermodynamic Database 12/07, 2014.

[48] B. Lothenbach, T. Matschei, G. Möschner, F.P. Glasser, Thermodynamic modelling of the effect of temperature on the hydration and porosity of Portland cement, Cem. Concr. Res. 38 (2008) 1–18, https://doi.org/10.1016/j.cemconres.2007.08.017.

[49] H.F.W. Taylor, Proposed structure for calcium silicate hydrate gel, J American Ceramic Society 69 (1986) 464–467, https://doi.org/10.1111/j.1151-2916.1986.tb07446.x.

[50] B. Lothenbach, D. Jansen, Y. Yan, J. Schreiner, Solubility and characterization of synthesized 11 Å Al-tobermorite, Cem. Concr. Res. 159 (2022) 106871, https://doi.org/10.1016/j.cemconres.2022.106871.

[51] Y. Fu, P. Xie, P. Gu, J.J. Beaudoin, Effect of temperature on sulphate adsorption/desorption by tricalcium silicate hydrates, Cem. Concr. Res. 24 (1994) 1428–1432.

[52] E. Gallucci, X. Zhang, K.L. Scrivener, Effect of temperature on the microstructure of calcium silicate hydrate (C-S-H), Cem. Concr. Res. 53 (2013) 185–195, https://doi.org/10.1016/j.cemconres.2013.06.008.

[53] B. Kolani, L. Buffo-Lacarrière, A. Sellier, G. Escadeillas, L. Boutillon, L. Linger, Hydration of slag-blended cements, Cem. Concr. Compos. 34 (2012) 1009–1018, https://doi.org/10.1016/j.cemconcomp.2012.05.007.

[54] J.I. Escalante-Garcia, Nonevaporable water from neat OPC and replacement materials in composite cements hydrated at different temperatures, Cem. Concr. Res. 33 (2003) 1883–1888, https://doi.org/10.1016/S0008-8846(03)00208-4.

[55] L. Huang, L. Tang, I. Löfgren, N. Olsson, Z. Yang, Real-time monitoring the electrical properties of pastes to map the hydration induced microstructure change in cement-based materials, Cem. Concr. Compos. 132 (2022) 104639.

[56] N. Schwarz, N. Neithalath, Influence of a fine glass powder on cement hydration: comparison to fly ash and modeling the degree of hydration, Cem. Concr. Res. 38 (2008) 429–436, https://doi.org/10.1016/j.cemconres.2007.12.001.

[57] A. Ipavec, R. Gabrovšek, T. Vuk, V. Kaučič, J. Maček, A. Meden, Carboaluminate phases formation during the hydration of calcite-containing Portland cement: Carboaluminate phase formation, J. Am. Ceram. Soc. 94 (2011) 1238–1242, https://doi.org/10.1111/j.1551-2916.2010.04201.x.

[58] T. Matschei, B. Lothenbach, F.P. Glasser, The role of calcium carbonate in cement hydration, Cem. Concr. Res. 37 (2007) 551–558.

[59] F. Georget, B. Lothenbach, W. Wilson, F. Zunino, K.L. Scrivener, Stability of hemicarbonate under cement paste-like conditions, Cem. Concr. Res. 153 (2022) 106692.

[60] K. De Weerdt, K.O. Kjellsen, E. Sellevold, H. Justnes, Synergy between fly ash and limestone powder in ternary cements, Cem. Concr. Compos. 33 (2011) 30–38, https://doi.org/10.1016/j.cemconcomp.2010.09.006.

[61] S.-C. Han, Y. Jo, J.-I. Yun, Chemical degradation of fly ash blended concrete with the seasonal variation of rainwater in a radioactive waste repository: a thermodynamic modeling approach, Cem. Concr. Res. 141 (2021) 106326, https://doi.org/10.1016/j.cemconres.2020.106326.

[62] J. Skibsted, E. Henderson, H.J. Jakobsen, Characterization of calcium aluminate phases in cements by aluminum-27 MAS NMR spectroscopy, Inorg. Chem. 32 (1993) 1013–1027.

[63] S.A. Bernal, J.L. Provis, B. Walkley, R. San Nicolas, J.D. Gehman, D.G. Brice, A. R. Kilcullen, P. Duxson, J.S.J. van Deventer, Gel nanostructure in alkali-activated binders based on slag and fly ash, and effects of accelerated carbonation, Cem. Concr. Res. 53 (2013) 127–144, https://doi.org/10.1016/j.cemconres.2013.06.007.

[64] S.-Y. Yang, Y. Yan, B. Lothenbach, J. Skibsted, Incorporation of sodium and aluminum in cementitious calcium-alumino-silicate-hydrate C-(A)-S-H phases studied by ^{23} Na, ^{27} Al, and ^{29} Si MAS NMR spectroscopy, J. Phys. Chem. C 125 (2021) 27975–27995, https://doi.org/10.1021/acs.jpcc.1c08419.

[65] I.G. Richardson, A.R. Brough, G.W. Groves, C.M. Dobson, The characterization of hardened alkali-activated blast-furnace slag pastes and the nature of the calcium silicate hydrate (C-S-H) phase, Cem. Concr. Res. 24 (1994) 813–829, https://doi.org/10.1016/0008-8846(94)90002-7.

[66] I.G. Richardson, The nature of C-S-H in hardened cements, Cem. Concr. Res. 29 (1999) 1131–1147, https://doi.org/10.1016/S0008-8846(99)00168-4.

[67] X. Cong, R.J. Kirkpatrick, 29Si MAS NMR study of the structure of calcium silicate hydrate, Adv. Cem. Based Mater. 3 (1996) 144–156.

[68] S.L. Poulsen, V. Kocaba, G. Le Saôut, H.J. Jakobsen, K.L. Scrivener, J. Skibsted, Improved quantification of alite and belite in anhydrous Portland cements by 29Si MAS NMR: effects of paramagnetic ions, Solid State Nucl. Magn. Reson. 36 (2009) 32–44, https://doi.org/10.1016/j.ssnmr.2009.05.001.

[69] P. Yu, R.J. Kirkpatrick, B. Poe, P.F. McMillan, X. Cong, Structure of calcium silicate hydrate (C-S-H): near-, mid-, and far-infrared spectroscopy, J. Am. Ceram. Soc. 82 (1999) 742–748.

[70] I.G. Richardson, G.W. Groves, The incorporation of minor and trace elements into calcium silicate hydrate (C-S-H) gel in hardened cement pastes, Cem. Concr. Res. 23 (1993) 131–138.

[71] K. Luke, E. Lachowski, Internal composition of 20-year-old fly ash and slag-blended ordinary Portland cement pastes, J. Am. Ceram. Soc. 91 (2008) 4084–4092.

[72] J.-I. Escalante-Garcia, J.H. Sharp, The chemical composition and microstructure of hydration products in blended cements, Cem. Concr. Compos. 26 (2004) 967–976, https://doi.org/10.1016/j.cemconcomp.2004.02.036.

[73] R. Taylor, I.G. Richardson, R.M.D. Brydson, Composition and microstructure of 20-year-old ordinary Portland cement–ground granulated blast-furnace slag blends containing 0 to 100% slag, Cem. Concr. Res. 40 (2010) 971–983, https://doi.org/10.1016/j.cemconres.2010.02.012.

[74] F.P. Glasser, J. Marchand, E. Samson, Durability of concrete — degradation phenomena involving detrimental chemical reactions, Cem. Concr. Res. 38 (2008) 226–246, https://doi.org/10.1016/j.cemconres.2007.09.015.

[75] A. Hidalgo, S. Petit, C. Domingo, C. Alonso, C. Andrade, Microstructural characterization of leaching effects in cement pastes due to neutralisation of their alkaline nature: part I: Portland cement pastes, Cem. Concr. Res. 37 (2007) 63–70.

[76] P.D. Tennis, H.M. Jennings, A model for two types of calcium silicate hydrate in the microstructure of Portland cement pastes, Cem. Concr. Res. 30 (2000) 855–863, https://doi.org/10.1016/S0008-8846(00)00257-X.

[77] R. Kurihara, I. Maruyama, Revisiting Tennis-Jennings method to quantify low-density/high-density calcium silicate hydrates in Portland cement pastes, Cem. Concr. Res. 156 (2022) 106786, https://doi.org/10.1016/j.cemconres.2022.106786.

[78] G.W. Scherer, D.M. Smith, Cavitation during drying of a gel, J. Non-Cryst. Solids 189 (1995) 197–211, https://doi.org/10.1016/0022-3093(95)00222-7.

[79] M. Rastogi, A. Müller, M.B. Haha, K.L. Scrivener, The role of cavitation in drying cementitious materials, Cem. Concr. Res. 154 (2022) 106710, https://doi.org/10.1016/j.cemconres.2022.106710.

[80] C. Zhou, X. Zhang, Z. Wang, Z. Yang, Water sensitivity of cement-based materials, J. Am. Ceram. Soc. 104 (2021) 4279–4296.

[81] H.M. Jennings, Refinements to colloid model of C-S-H in cement: CM-II, Cem. Concr. Res. 38 (2008) 275–289, https://doi.org/10.1016/j.cemconres.2007.10.006.

[82] P.A. Bonnaud, Q. Ji, B. Coasne, R.J.-M. Pellenq, K.J. Van Vliet, Thermodynamics of water confined in porous calcium-silicate-hydrates, Langmuir 28 (2012) 11422–11432, https://doi.org/10.1021/la301738p.

[83] M. Wyrzykowski, P.J. McDonald, K.L. Scrivener, P. Lura, Water redistribution within the microstructure of cementitious materials due to temperature changes studied with [1] H NMR, J. Phys. Chem. C 121 (2017) 27950–27962, https://doi.org/10.1021/acs.jpcc.7b08141.

[84] A.M. Gajewicz-Jaromin, P.J. McDonald, A.C.A. Muller, K.L. Scrivener, Influence of curing temperature on cement paste microstructure measured by 1H NMR relaxometry, Cem. Concr. Res. 122 (2019) 147–156, https://doi.org/10.1016/j.cemconres.2019.05.002.

[85] S. Brunauer, P.H. Emmett, E. Teller, Adsorption of gases in multimolecular layers, J. Am. Chem. Soc. 60 (1938) 309–319, https://doi.org/10.1021/ja01269a023.

[86] N. De Belie, J. Kratky, S. Van Vlierberghe, Influence of pozzolans and slag on the microstructure of partially carbonated cement paste by means of water vapour and nitrogen sorption experiments and BET calculations, Cem. Concr. Res. 40 (2010) 1723–1733, https://doi.org/10.1016/j.cemconres.2010.08.014.

[87] I.G. Richardson, Tobermorite/jennite-and tobermorite/calcium hydroxide-based models for the structure of CSH: applicability to hardened pastes of tricalcium silicate, β-dicalcium silicate, Portland cement, and blends of Portland cement with blast-furnace slag, metakaolin, or silica fume, Cem. Concr. Res. 34 (2004) 1733–1777.

[88] W. Kunther, S. Ferreiro, J. Skibsted, Influence of the Ca/Si ratio on the compressive strength of cementitious calcium–silicate–hydrate binders, J. Mater. Chem. A 5 (2017) 17401–17412.

[89] A.C.A. Muller, K.L. Scrivener, J. Skibsted, A.M. Gajewicz, P.J. McDonald, Influence of silica fume on the microstructure of cement pastes: new insights from 1H NMR relaxometry, Cem. Concr. Res. 74 (2015) 116–125.

[90] J.E. Rossen, B. Lothenbach, K.L. Scrivener, Composition of C–S–H in pastes with increasing levels of silica fume addition, Cem. Concr. Res. 75 (2015) 14–22.

[91] T. Katayama, The so-called alkali-carbonate reaction (ACR) — its mineralogical and geochemical details, with special reference to ASR, Cem. Concr. Res. 40 (2010) 643–675, https://doi.org/10.1016/j.cemconres.2009.09.020.

[92] B. Walkley, R. San Nicolas, M.-A. Sani, G.J. Rees, J.V. Hanna, J.S.J. Van Deventer, J.L. Provis, Phase evolution of C-(N)-A-S-H/N-A-S-H gel blends investigated via alkali-activation of synthetic calcium aluminosilicate precursors, Cem. Concr. Res. 89 (2016) 120–135, https://doi.org/10.1016/j.cemconres.2016.08.010.

[93] G.W. Brindley, S. Kikkawa, A crystal-chemical study of Mg, Al and Ni, N hydroxy-perchlorates and hydroxycarbonates, Am. Mineral. 64 (1979) 836–843.

[94] W. Stumm, J.J. Morgan, Aquatic Chemistry: Chemical Equilibria and Rates in Natural Waters, John Wiley & Sons, 2012.

[95] F. Morel, Principles of Aquatic Chemistry (No Title), 1983.

[96] M. Zilberbrand, On equilibrium constants for aqueous geochemical reactions in water unsaturated soils and sediments, Aquat. Geochem. 5 (1999) 195–206.

[97] E.A. Guggenheim, The theoretical basis of Raoult's law, Trans. Faraday Soc. 33 (1937) 151, https://doi.org/10.1039/tf9373300151.

[98] H. Chen, M. Wyrzykowski, K. Scrivener, P. Lura, Prediction of self-desiccation in low water-to-cement ratio pastes based on pore structure evolution, Cem. Concr. Res. 49 (2013) 38–47, https://doi.org/10.1016/j.cemconres.2013.03.013.

[99] F.J. Millero, Molal volumes of electrolytes, Chem. Rev. 71 (1971) 147–176.

[100] A. Vollpracht, B. Lothenbach, R. Snellings, J. Haufe, The pore solution of blended cements: a review, Mater. Struct. 49 (2016) 3341–3367.

[101] M. Volmer, A. Weber, Keimbildung in übersättigten Gebilden, Z. Phys. Chem. 119 (1926) 277–301.

[102] S. Garrault-Gauffinet, A. Nonat, Experimental investigation of calcium silicate hydrate (C-S-H) nucleation, J. Cryst. Growth 200 (1999) 565–574, https://doi.org/10.1016/S0022-0248(99)00051-2.

[103] K.-J. Wu, E.C.M. Tse, C. Shang, Z. Guo, Nucleation and growth in solution synthesis of nanostructures – from fundamentals to advanced applications, Prog. Mater. Sci. 123 (2022) 100821, https://doi.org/10.1016/j.pmatsci.2021.100821.

[104] D. Kashchiev, Nucleation, Elsevier, 2000.

[105] D. Kashchiev, G.M. van Rosmalen, Review: nucleation in solutions revisited, Cryst. Res. Technol. 38 (2003) 555–574, https://doi.org/10.1002/crat.200310070.

[106] S.-Y. Hong, F.P. Glasser, Alkali sorption by C-S-H and C-A-S-H gels part II. Role of alumina, Cem. Concr. Res. 32 (2002).

[107] Y. Yan, B. Ma, G.D. Miron, D.A. Kulik, K. Scrivener, B. Lothenbach, Al uptake in calcium silicate hydrate and the effect of alkali hydroxide, Cem. Concr. Res. 162 (2022) 106957, https://doi.org/10.1016/j.cemconres.2022.106957.

[108] T.T.H. Bach, C.C.D. Coumes, I. Pochard, C. Mercier, B. Revel, A. Nonat, Influence of temperature on the hydration products of low pH cements, Cem. Concr. Res. 42 (2012) 805–817.

[109] C.J. Stephens, S.F. Ladden, F.C. Meldrum, H.K. Christenson, Amorphous calcium carbonate is stabilized in confinement, Adv. Funct. Mater. 20 (2010) 2108–2115, https://doi.org/10.1002/adfm.201000248.

[110] C. Labbez, L. Bouzouaid, A.E.S. Van Driessche, W.L. Ling, J.C. Martinez, B. Lothenbach, A. Fernandez-Martinez, Mechanisms and kinetics of C-S-H nucleation approaching the spinodal line: insights into the role of organics additives, Cem. Concr. Res. 173 (2023) 107299, https://doi.org/10.1016/j.cemconres.2023.107299.

[111] X.M. Aretxabaleta, J. López-Zorrilla, I. Etxebarria, H. Manzano, Multi-step nucleation pathway of C-S-H during cement hydration from atomistic simulations, Nat. Commun. 14 (2023) 7979, https://doi.org/10.1038/s41467-023-43500-y.